LONG-RANGE DIPOLAR FIELDS AS A TOOL FOR NUCLEAR MAGNETIC RESONANCE MICROSCOPY

by

Wei Dong

B.S. (Fudan University, China) 2002

M. Phil. (Graduate Center of The City University of New York) 2006

A dissertation submitted to the Graduate Faculty in Physics in partial fulfillment of the requirements for the degree of Doctor of Philosophy, The City University of New York

2009

This manuscript has been read and accepted for the graduate faculty in Physics in satisfaction of the dissertation requirement for the degree of Doctor of Philosophy

Prof. **Carlos Meriles**

_____ _____

Chair of Examining Committee Date

Prof. **Steven Greenbaum**

_____ _____

Executive Officer Date

Supervisory Committee:

Prof. Carlos Meriles, Department of Physics, CCNY

Prof. Alexej Jerschow, Department of Chemistry, NYU

Prof. Hernan Makse, Department of Physics, CCNY

Prof. Sergey Vitkalov, Department of Physics, CCNY

The Graduate School and University Center

Of

The City University of New York

ABSTRACT

Long-Range Dipolar Fields as a Tool for Nuclear Magnetic Resonance Microscopy

By

Wei Dong

Mentor: Prof. Carlos Meriles

Nuclear Magnetic Resonance (NMR) is widely used today for structural and dynamical studies of the properties of diverse materials. However, due to the relatively low sensitivity of the standard induction detection method, NMR is strongly constrained when probing samples whose effective dimensions are less than a few microns. To overcome these limitations, our novel strategy based on the manipulation of the long-range dipolar interactions between the sample and a hyperpolarized semiconductor tip located close to its surface. These interactions are used to modulate the tip nuclear magnetization in a way proportional to the local sample magnetization. The advantage of this strategy lies in that the highly sensitive detection methods – e.g., optical detection – can be used to monitor the semiconductor tip, thus providing the opportunity to indirectly probe the sample neighboring the tip with a favorable signal-to-noise ratio. Because the detected portion of the sample is comparable to the size of the tip, resolution exceeding the currently attainable could be possible.

As an initial demonstration of our methodology we designed an experiment in which a 3 mm diameter distilled water droplet – playing the role of a sensor – was used to detect the NMR signal of the sample surrounding the droplet, in this case, silicon oil (Sigma-Aldrich) contained in a 5 mm diameter glass tube. Notice the sample (oil) and the detection center (water) are distinct and discernible objects only connected through long range intermolecular dipolar couplings. A special pulse sequence was designed and applied in the experiment to encode the sample magnetization for detection. By utilizing the Runge-Kutta algorithm, I modeled a 2000 spins ensemble based on the given geometry and numerically calculated the Bloch differential equations of this coupled spins system. Experimental results have a very good agreement with the numerical calculations. This preliminary experiment proves that not only the sample NMR signal can be indirectly detected, also many other sample information – e.g., relaxation time, sample spectrum, etc. – are attainable.

Minimizing the short range dipolar couplings is a very crucial part to achieve the final goal of this strategy when the solid state semiconductor was used as the sensor. At the second stage, a modified MREV16 decoupling pulse sequence was designed and applied to greatly reduce the short range dipolar couplings inside the solid state sensor. A 3 mm thick disk GaAs crystal has been chosen as the sensor due to its excellent optical hyperpolarization properties. By acquiring ^{71}Ga NMR signal, I successfully indirectly detected a tiny nuclear dipolar field induced by proton spins from an adjacent organic sample (as small as 7 nT). Optical enhancing the bulk averaged nuclear spin polarization in semiconductors is another critical technique that will be integrated into our strategy. Comparing to the thermal nuclear magnetization, we achieved 2-3 orders of magnitude

optical enhancement for ^{71}Ga in GaAs crystal and 3 orders for ^{125}Te in CdTe crystal. Finally optical Faraday rotation will be used as an ultrasensitive detection to incorporate into the strategy. Optical reading of the electronic Larmor frequency shift in the semiconductor by using Time-Resolved Faraday Rotation (TRFR) to probe the sample magnetization change is the basic idea of our optical detection scheme.

Through collaboration with Attocube AG, a leading company specialized on low temperature optical microscopy, our cutting-edge cryogenic optical NMR probe has been finished. Certainly, integrating optical hyperpolarization and optical detection with modern NMR technique is very challenging and requires tremendous work. However given the steady progress in the area of nanotechnology, our strategy's future still appears quite promising.

Acknowledgement

As time flies away, it's almost seven years that I have spent in doing my Ph.D. study. To me, these years' study and research work are much like a spiritual journey into the magnificent palace of physics and I truly enjoy the wonders with every step I made. I know how lucky I am. Because during this journey I have met one person from whose enlightenments and inspirations I will benefit all my life. He is my academic mentor, Prof. Carlos Meriles. Carlos not only has taught me what nuclear magnetic resonance is, what the physicists "gut feelings" are, as well as how to analyze and solve difficulties in research, but also has demonstrated me how diligent we should be and how positive attitude we should have to face our lives. I have even learnt from him a lot how to speak and write English more properly. I know I'm indebted to Carlos too much to speak with words. Only my heart knows how badly I wish I could stay in his group longer.

I'm grateful to Dr. Phillip Stallworth for his patient instructions how to do the basic NMR experiments when I was first exposed to NMR technique environment.

I truly treasure those study time with Hao Jiang.

I also thank Dr. Boris Itin for his help and advice when I ran the experiments at New York Structural Biology Center.

I really enjoy all the time with Dr. Bo Li when we did the optical pumping NMR experiments. I will never forget the day you drove me to hospital because I was sick after a non-stopped 24 hours experiment work.

I'd like to express my cordial thank to Daniela Pagliero. I have a great time to work with you on the optical detection of nuclear magnetization experiment.

I'd also like to thank Yunpu for her assistance and help in the lab.

Finally I'd like to express my special appreciation to my girlfriend Helen. I could imagine how lonely and miserable my life would be, if I didn't have your supports and your love. And I know for sure I couldn't make it without my mother Yulan and my father Jianfa's selfless and forever supports. I feel truly lucky I can have parents as you are.

Contents

List of Figures

List of Symbols

Common Physical Constants

k	Boltzmann's Constant
h	Planck's Constant
$\hbar$	$h/2\pi$

Properties of Spins

$\vec{\mu}_n$	magnetic moment of the nucleus
γ	gyromagnetic ratio
g^*	Landé factor

External Magnetic Fields

$\vec{B}$	total external field
$\vec{B}_0$	static component of $\vec{B}$, oriented along the z−axis
$\vec{B}_1$	oscillating component of $\vec{B}$, induced by pulses on the xy−plane
μ_B	Bohr magneton

Acronyms and Abbreviations

NMR	Nuclear Magnetic Resonance
TRFR	Time-resolved Faraday rotation
OFR	Optical Faraday rotation
ODNMR	Optically Detected Nuclear Magnetic Resonance
OPNMR	Optically Pumped Nuclear Magnetic Resonance
DFM	Dipolar Field Microscopy
DC	Direct Current
rf	radio frequency
MBE	Molecular Beam Epitaxy
a.u.	arbitrary units

Semiconductors

GaAs	Gallium Arsenide
CdTe	Cadmium Tellurium
InP	Indium Phosphide
CdS	Cadmium Sulfide

Chapter 1

Introduction

Nuclear magnetic resonance (NMR) is unarguably one of the most powerful techniques available today to characterize diverse systems, widely used in many different fields. Not only has its importance been demonstrated in chemistry and physics, but the usefulness of NMR has also deeply impacted the world of biology and medicine. In order to provide sufficient background knowledge to understand NMR phenomenon, I will start this chapter with a brief review in fundamentals and physics underlying of NMR. And then the current NMR major constrains – the limited sensitivity of NMR spectroscopy will be covered. As an end of the chapter, an introduction of our novel strategy – Dipolar Field Microscopy (DFM) – will be elaborated.

1.1 Nuclear Magnetic Resonance

Many nuclei isotopes, such as ^{1}H, ^{13}C, ^{15}N, ^{19}F, ^{31}P, ^{71}Ga, and ^{125}Te possess non-zero intrinsic magnetic moments $\vec{\mu}_n$. All experimental evidence concerning the magnetic properties of nuclei is consistent with the hypothesis that the magnetic moment $\vec{\mu}_n$ is proportional and parallel to its intrinsic angular momentum or spin $\vec{I}$,

$$\vec{\mu}_n = \gamma \hbar \vec{I} \tag{1.1}$$

where γ is the well-known gyromagnetic ratio which is the "finger print" of the particle. In the presence of a magnetic field, $\vec{B}$, the energy $\vec{H}$ of the nucleus is determined by the magnitude and by the relative orientation of magnetic moment with the field:

$$\vec{H} = -\vec{\mu}_n \cdot \vec{B} \tag{1.2}$$

In typical magnetic resonance experiment, there are several sources which can contribute to $\vec{B}$, however external magnetic field $\vec{B}_0$ along the z-axis is usually the most dominant part. According to Quantum Mechanics, we know that the nuclear spin's z-component $\vec{I}_z$ is only allowed to be one of $2I+1$ distinct states in which the components have values equal to $-I, (-I+1), ..., (I-1), I$. These values are well known as magnetic quantum number m. Hence the dominant energy due to external field is given by,

$$H_z = -\gamma \hbar m B_0 = -\Delta E_m m \tag{1.3}$$

H_z is also called Zeeman Hamiltonian. $\Delta E_m = \gamma \hbar B_0$ is the energy separation between two adjacent eigenstates. Commonly speaking, for a Tesla order magnetic field, the resonance frequency $\nu_0 = \frac{\Delta E_m}{h}$ is in the radio frequency (rf) region of the electromagnetic spectrum. That is why we usually call the excitation pulse rf pulse in NMR.

For simplicity purpose, let us consider one NMR experiment in which the contribution to $\vec{B}$ only comes from the large external magnetic $\vec{B}_0$. This approximation actually is reasonable, since the overall behavior of nuclear spins in a magnetic resonance experiment is determined by the Zeeman part. When nuclear spins are in thermal equilibrium, the system tries to populate spins to the lowest possible energy state, as a

result the overall magnetization of the system is aligned with $\vec{B}_0$. This bulk-averaged nuclear spin magnetization is usually denoted by $\vec{M}$. A time-varying magnetic field $\vec{B}_1$, perpendicular to $\vec{B}_0$ induced by a coil around the sample, can deflect $\vec{M}$ from its thermal equilibrium direction, if $\vec{B}_1$ oscillates near the nuclei resonance frequency ($\omega_0 = \gamma B_0$). In conventional NMR the detection coil is the same excitation coil which is also a part of the detection circuit and has to be tuned precisely to the resonance frequency ω_0. When $\vec{M}$ processes about the z-axis, an induced voltage is collected by the coil and sent to the spectrometer. This voltage will decay with time and is commonly termed "the free-induced decay (FID)." It is worth pointing out that the processing nuclear magnetization originates from a coherent superposition of nuclear spin eigenstates and FID is a result of decoherence between the spins. Fourier transformation of the FID yields the NMR spectrum. All above mentioned basically outlined a 'single pulse' NMR experiment.

1.2 The limited sensitivity of NMR spectroscopy

As well known, NMR signal intensity is proportional to the nuclear spin magnetization $\vec{M}$, which means the greater $\vec{M}$ we can achieve, the higher sensitivity of NMR spectroscopy is. However nuclear spin magnetization $\vec{M}$ is quite low even in a Tesla order magnet. In order to illustrate this point, let us calculate the ensemble average expectation value of I_z, $< I_z >$. By using Boltzmann statistics $< I_z >$ at thermal equilibrium can be written as

$$< I_z >= \frac{\sum_m i_{z,m} e^{-\frac{E_m}{kT}}}{\sum_m e^{-\frac{E_m}{kT}}} \tag{1.4}$$

where $i_{z,m}$ and E_m are the m-th eigenvalue of angular momentum I_z and energy H_z respectively. Since $E_m = -\Delta E_m m$, Eq. 1.4 can be rewritten as

$$< I_z >= \frac{\sum_m m e^{\frac{m\Delta E_m}{kT}}}{\sum_m e^{\frac{m\Delta E_m}{kT}}} \tag{1.5}$$

For a case of spin ½ ^{125}Te nuclei,

$$< I_z >= \frac{-\frac{1}{2} e^{-\frac{\Delta E_m}{2kT}} + \frac{1}{2} e^{\frac{\Delta E_m}{2kT}}}{e^{-\frac{\Delta E_m}{2kT}} + e^{\frac{\Delta E_m}{2kT}}} = \frac{1}{2}\tanh(\frac{\hbar\gamma B_0}{2kT}) \tag{1.6}$$

Substituting the typical value of $\gamma_{^{125}Te} = 8.41\times10^7$ rad T^{-1} S^{-1} and $B_0 = 9.4$ T into Eq. 1.6, we can obtain that, at room temperature $T = 300K$, $< I_z >$ equals 5.03×10^{-6}, which means only 1 out of 198,700 ^{125}Te nuclei will be aligned along with z-axis. Meanwhile because the magnitude of nuclear spin magnetization $\vec{M}$ is proportional to $< I_z >$, finally we see the low sensitivity of NMR spectroscopy originates from the insufficiency of initial nuclear spin magnetization $\vec{M}$. Practically speaking, in order to render a detectable NMR signal, a sample typically must contain at least 10^{18} nuclear spins, and even then signal averaging for hours, if not days, is often required. As a result, dilute spin systems (e.g., surface atoms and atoms at defect sites) are usually inaccessible to solid state NMR.

1.3 Introduction of Dipolar Field Microscopy (DFM) Strategy

Let us consider the setup in Fig. 1.1: an intense external magnetic field uniformly polarizes an extended sample in the direction perpendicular to its surface. Close to this surface is a semiconductor tip previously hyper-polarized by optical pumping (with either a cw or pulsed circularly polarized laser beam). The setup also includes a radio-frequency (rf) coil to manipulate the evolution of the spin system in the sample and in the tip. For *simplicity* (Meriles)[1], it has been assumed that the hyperpolarized region is spherical with radius a, and that its center is located a distance d from the surface of the sample. In this case, the tip induces a dipolar magnetic field of the form

$$\mathbf{B}_{tip} = \frac{\mu_0}{3r'^3}\left(\frac{a}{d}\right)^3 \left(3\left(\mathbf{M}_{tip}^{(0)} \cdot \hat{\mathbf{r}}'\right)\hat{\mathbf{r}}' - \mathbf{M}_{tip}^{(0)}\right) \tag{1.7}$$

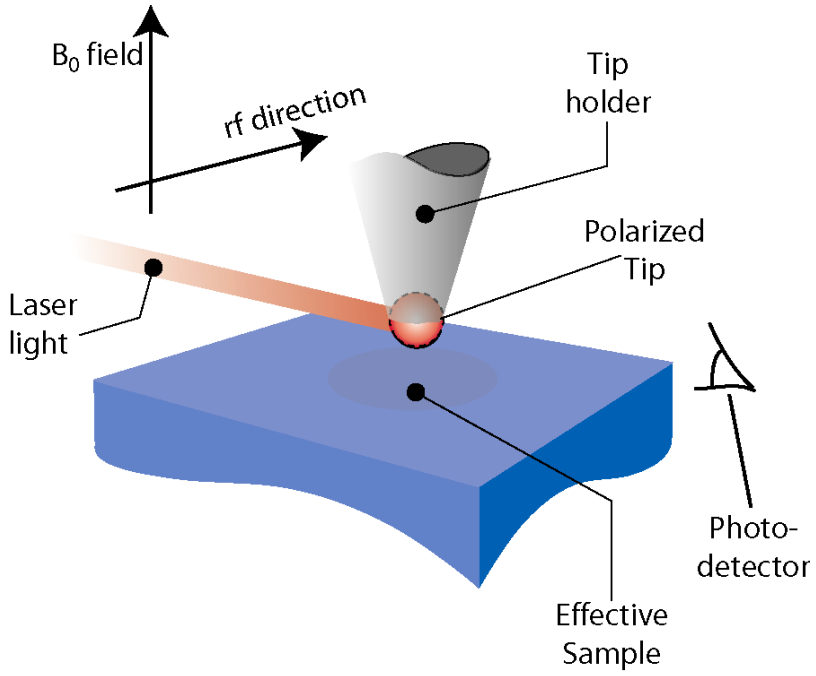

Fig.1.1 Basic experimental setup

$\mathbf{M}_{tip}^{(0)}$ represents the (pumped) nuclear magnetization in the tip (collinear with the external field) μ_0 is the vacuum magnetic permeability and **r'** is the vector from the sample to the center of the sphere; the prime indicates that the coordinates have been expressed in units of the distance *d*. The spatial variation of the dipolar field can be used to select the sample region to be studied. Let us consider, for instance, the rf pulse sequence $(\pi/2)_y - t_{c1} - (\pi/2)_x$ acting on the sample nuclei. As usual in NMR, the sub-index in each pulse indicates the rf phase in the rotating frame; t_{c1} represents the variable evolution interval between the pulses. *For ease in presentation only, we will first ignore any other spin interactions taking place simultaneously* (i.e., *J*-couplings, homo- and heteronuclear dipolar interactions with other spins in the sample, chemical shifts, etc.). Having made this assumption, a simple calculation shows that, at the end of the sequence, the magnetization along the *z*-direction (parallel to the external magnetic field) is given by

$$\mathbf{M}_{spl}^{(z)}(t_{c1}) = \mathbf{M}_{spl}^{(0)} \sin\left(\gamma_{spl} t_{c1} (B_{tip})_z\right) \tag{1.8}$$

$\mathbf{M}_{spl}^{(0)}$ represents the equilibrium magnetization in the sample and γ_{spl} is the nuclear gyromagnetic ratio of the probed nuclei. Finally, $(B_{tip})_z = (B_{tip}^{\max}/2r'^5)(3z'^2 - r'^2)$ is the *z*-component of the dipolar field due to the tip in primed coordinates; $B_{tip}^{\max} = (2\mu_0/3)M_{tip}^{(0)}(a/d)^3$ is the maximum value of this field over the sample. The use of the dipolar field due to the tip to control the distribution of magnetization in the sample can be directly visualized in Fig. 1.2.

In case A, the inter-pulse interval t_{c1} has been chosen such that $\gamma_{spl} t_{c1} B_{tip}^{max} = \pi/2$. The result is the concentration of magnetization in the region closest to the tip. As inferred from the figure, this volume is basically proportional to d^3 indicating that the magnetization becomes more localized as the center of the hyperpolarized sphere moves closer to the sample surface.

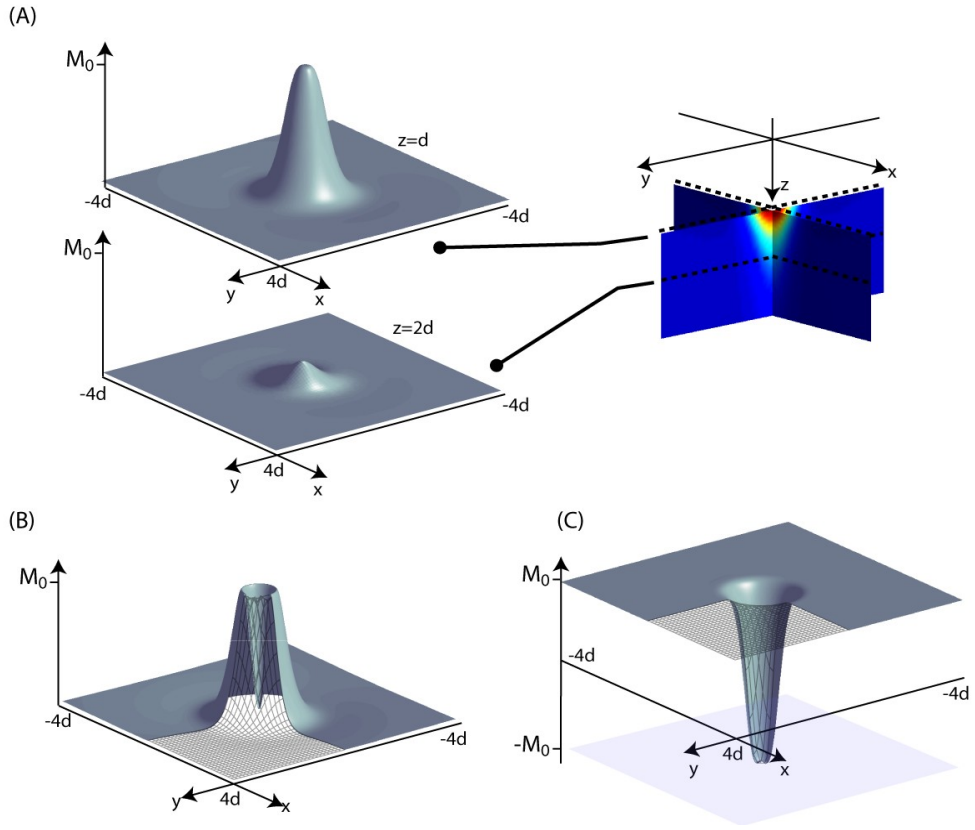

Fig. 1.2: (A) Numerical results indicating the sample magnetization after the pulse sequence 90y-tc1-90x. (B) Idem as in (A) but with the second pulse doubled. (C) As in (B) but with the phase of the second pulsed changed to *–y*.

A crucial consequence of this inhomogeneous distribution of sample magnetization is that it induces a rather strong dipolar field at the site of the tip, which, in the case discussed above, reaches a magnitude[4] $B_{spl}^{\max} = 0.6\mu_0 M_{spl}^{(0)} / (4\pi)$. To more fully appreciate this result it is important to bear in mind *that the dipolar field of a uniformly magnetized infinite layer vanishes*.[2,3] This can be seen by considering a point located a distance *d* above the layer, whereby the dipolar field due to the nuclei in a central disk of radius $\sqrt{2}d$ is anti-parallel to the field generated by nuclei outside this disk. The exact cancellation upon the superposition of both contributions is a non-intuitive and somewhat fortuitous result: the dipolar field of each individual spin diminishes with the distance to the center of the disk; however, the number of equally contributing spins increases with the square of this distance. The nulling of the total dipolar field is the result of a delicate equilibrium involving regions of the sample that are far apart from each other.[*] The magnetization distribution obtained for the case shown in Fig. 1.2 implies that, after the preparation sequence, only those nuclei within the central disk will contribute to the dipolar field in the tip. However, it is possible to alter the parameters of the preparation sequence to generate, for instance, a dipolar field of comparable magnitude, this time only due to nuclei outside the central disk (Fig 1.2C) or in a ring around its center (Fig. 1.2B). This versatility confers to this scheme very singular properties that can be used to selectively get information from complementary regions.

---

* A ring of spins complementary to the central disk and having an outer radius roughly 40 times greater than its inner radius will reduce the total dipolar field at the center of the tip to 10% the value due only to the central disk.

The detection of the sample magnetization by means of the tip is carried out in analogous fashion with that of the preparation period. At the end of the pulse sequence $(\theta)_y - t_{c2} - (\theta)_x$, it can be shown that the *z*-component of the magnetization in the tip is given by

$$\mathbf{M}_{tip}^{(z)}\left(t_{c2}\right) = \mathbf{M}_{tip}^{(0)}\left(1-\sin^2\theta\left(1-\sin\left(\frac{\pi}{2}\frac{\left(B_{spl}\right)_z}{\left(B_{spl}^{\max}\right)_{ref}}\right)\right)\right) \tag{1.9}$$

Here, the contact time t_{c2} has been chosen so that $\gamma_{tip} t_{c2}\left(B_{spl}^{\max}\right)_{ref} = \pi/2$. In this formula, $\left(B_{spl}^{\max}\right)_{ref}$ represents the (peak) dipolar field created by a reference sample (of optimum nuclear density) at the site of the tip. Formula (3) implies that at the end of the second time interval, the tip magnetization becomes modulated by the changes of the dipolar field $\left(B_{spl}\right)_z$, which, in turn, depends on the magnetization of the selected sample region. Thus, an optical inspection of the electronic spin precession in the semiconductor tip reveals a shift (with respect to the Larmor frequency as measured prior to manipulating the tip nuclei) equal to

$$\Delta f = kM_{tip}^{(0)}\sin^2\theta\left(1-\sin\left(\frac{\pi}{2}\frac{\left\langle M_{spl}\right\rangle}{M_{spl}^{ref}}\right)\right) \tag{1.10}$$

For the case of Fig. 1.2A, $\left\langle M_{spl}\right\rangle$ represents the average magnetization in a hemisphere of radius ~d located immediately close to the tip and M_{spl}^{ref} is simply a scale factor interpreted as the magnetization in the same volume with best conceivable nuclear density (reference sample). Eq. (1.10) implies that, in principle, one can probe the local

magnetization of the sample by optically inspecting the tip. Interestingly enough, the signal to noise of the measurement only depends on our ability to detect changes of the electronic precession frequency in the semiconductor. This, in turn, rests on the amplitude of the nuclear magnetization in the tip and the electronic de-coherence time, parameters that can be advantageously selected, as shown below.

Crucial in the detection scheme described so far is the adequate control of the short-range spin interactions that take place in a solid at the low temperatures necessary for optical pumping. A similar requirement is encountered in solid-state imaging[4] or in experiments that measure spin diffusion in a solid.[5] Here, multiple pulse coherent averaging is employed to suppress undesired spin-spin interactions during the creation of magnetization gratings by the pulsed field gradients. A similar approach can be used in the present case and is shown in Fig. 1.3. From a practical standpoint, the finite amplitude and spatial inhomogeneities of the radio-frequency (rf) field impose a limit to the time during which it is possible to preserve coherence in the spin evolution of a solid system. In static *protonated* samples, where the homonuclear dipolar interaction is particularly intense, this time is at most a few milliseconds (in a macroscopic sample).[6] It follows from here that the modulation of the tip magnetization (and consequently, the detection sensitivity) will be optimized when the contact times between the tip and the sample are kept within this limit. For a tip having a curvature radius slightly larger than half the distance to the surface ($a/d \approx 0.7$) and polarized to 10% (or 30%), a very conservative numerical analysis yields a preparation contact time $t_{c1} \approx 1$ ms (or 0.33 ms). Notice, however, that due to the cubic dependence with the distance, this value reduces to only

~300 μs (or 100 μs) when the tip rests just above the sample surface $(a \approx d)$.[1] The contact time required during the encoding period t_{c2} is inversely proportional to the sample magnetization. For a densely protonated sample in a magnetic field of 14 T (600 MHz proton frequency) and at 4 K, Eqn. (6) yields $t_{c2} \approx 1/\gamma_{tip} B_{spl}^{\max} \approx 75$ ms. This value is within the decoherence time of the nuclei in the semiconductor tip. This is because the comparatively lower value of the gyromagnetic ratio γ_{tip} leads to weaker dipolar interactions, which, accordingly, can be efficiently decoupled during longer times.

From a general perspective, the point-by-point reconstruction of the resonance spectrum does not significantly differ from the one used in other schemes of indirect detection. Recent examples are the encoding and "remote" detection of hyperpolarized xenon[9] or the reconstruction of nuclear magnetic resonance spectra detected by a mechanical oscillator in a "gradient-free" permanent magnet.[10] Notice that, in the presented method, the point-by-point reconstruction during the final optical reading period is not a significant inconvenience since the electronic relaxation is very fast (τ_{elec}<1 μs). On the other hand, because detection is carried out at low temperatures, long nuclear relaxation times (reaching in some cases several tens of minutes) do represent an important limitation that has to be taken into account. There are several tools that can be used to mitigate this problem: for example, for a given signal to noise ratio, the inspection angle θ in the tip diminishes the stronger the polarization (or the longer the electronic relaxation time). It follows that, ideally, only a small fraction of the tip magnetization should be recovered after each observation. On the other hand, the addition

of paramagnetic impurities could be used to control the sample relaxation although, in biological samples, proton relaxation is usually fast enough.[11]

Chapter 2

Indirect Detection of NMR via Geometrically Induced Long-Range Dipolar Fields in Liquid

2.1 Abstract

We report the indirect detection of the magnetization of one spin species via the NMR signal of a second species. Our method relies on the control of long-range dipolar fields between two separate objects, in this case, a water droplet (sensor) immersed in a tube containing mineral oil (sample). Unlike prior experiments, no gradient pulses are used; rather, the setup geometry is exploited to select the part of the sample to be probed and modulate the spin alignment in the sensor. Our results are discussed in the context of Dipolar Field Microscopy, a proposed strategy in which the detector is a hyperpolarized tip.

2.2 Overview

Collective effects of the nuclear magnetization on the NMR spin dynamics were first reported by Deville, Bernier, and Delrieux[12]. In an experiment conducted almost thirty years ago, they observed and explained the unexpected string of echoes, following a standard two-pulse sequence in hyperpolarized ^{3}He. With the advent of improved higher-field NMR systems, non-linear nuclear spin dynamics became the subject of renewed attention as substantial effects were observed in protonated solutions at room temperature[13]. In the early 90's, Bowtell proposed a method for the indirect detection of one spin species via the demagnetizing field produced by spins in solution of a different species. Unlike other schemes, spins do not need to be part of the same molecule; in fact, the only requirement is that the two nuclear species be sufficiently close [14]. Extending these ideas, Warren et al.[15,16] and Bowtell et al.[17] showed that interactions can be established between nuclei of high gyro-magnet ratios located in separate containers. In all these experiments, gradient pulses were used throughout the sequence to break the symmetry of the sample polarization by inducing a helical distribution of magnetization along the gradient pulse direction. A non-zero dipolar field is thus created and used to couple the analyte and the sensor nuclei. Broadly speaking, contributions to the dipolar field at every point originate mostly from nuclei contained in a sphere having a radius equal to the helix pitch[18]. Therefore, if sample and sensor nuclei reside in separate containers, the amount of coupling (i.e., the dipolar field of one nuclear species acting on the other) can be controlled by the duration of the gradient pulse. Recently, Meriles proposed that long-range dipolar couplings could serve as a tool for NMR microscopy[1]. In this scheme, the dipolar field of a small hyperpolarized tip placed in close contact with

an extended sample is used to reorient the sample magnetization in the neighborhood of the tip. The result is a strong dipolar field at the tip site—this time, due to the sample—which is used in a second stage to modulate the tip magnetization. This approach could prove advantageous because highly sensitive methods can be used to probe the microtip and thereby, indirectly probe the sample with a resolution comparable to the size of the tip.

2.3 Methods and Results

As an initial demonstration of this methodology, we designed an experiment in which a 3 mm diameter distilled water droplet—playing the role of the sensor—was used to detect the NMR signal of the sample surrounding the droplet, in the present case, silicone oil (Sigma – Aldrich) contained in a 5 mm diameter glass tube. Despite the change in geometry (the detection center is now embedded in the sample), the basic assumption of the scheme described above still holds: the sample (oil) and the detection center (water) are distinct and separate objects only connected through long-range intermolecular dipolar couplings. The scheme is reminiscent of previous work carried out by Pines and collaborators[19], who showed that hyperpolarized Xenon can be used as a sensor to pick up the signal of an analyte located in a separate container. Also, long-range dipolar fields in oil-water emulsions have been studied in the past by Cory and coworkers[20]. Nonetheless, the context and motivation are markedly different in this experiment. Furthermore, our strategy uses only the geometry of the setup to generate

and detect the dipolar field interaction, i.e. no symmetry-breaking field gradient pulses are utilized.

Fig. 2.1 shows the pulse sequence used: selective excitation of the oil protons initiates the evolution of the sample magnetization in the presence of the dipolar field due to the water droplet. In the frame rotating at the oil Larmor frequency, only nuclei neighboring the water droplet are affected by its dipolar field. The contact time $t_{c1} = 3\pi/\left(4\gamma\mu_0 M_{det}^0\right)$ is chosen so that sample nuclei located close to the poles of the water droplet total a π/2 rotation during the first interval. In the above expression, M_{det}^0 is the equilibrium magnetization of the detector, γ is the proton gyromagnetic ratio and μ_0 is the vacuum magnetic permeability. In a magnetic field of 9.4 T (400 MHz ^{1}H resonance frequency) at room temperature we have t_{c1}~300 ms. It is not difficult to demonstrate that the sample magnetization parallel to the main magnetic field (z-axis) at the end of the encoding period is given by

$$M_{spl}^{(z)}\left(t_{c1}\right) = M_{spl}^0 \sin\left(\frac{\pi}{4}\left(\frac{r_0}{r}\right)^3\left(3\cos^2\theta - 1\right)\right) \tag{2.1}$$

Here, M_{spl}^0 is the equilibrium sample magnetization; r_0 is the water droplet radius; r is the distance to the droplet center and h is the angle with the main magnetic field direction. The strongly inhomogeneous distribution of sample magnetization induces a rather homogeneous dipolar field on the water droplet. A full numerical calculation shows that this field reaches a magnitude equal to $B_{spl}^{\max} = 2.3\mu_0 M_{spl}^{(0)}/\left(4\pi\right)$ with a variation of

approximately $\pm 10\%$ over the droplet volume. At 9.4 T for a room-temperature silicone-oil sample, $B_{spl}^{\max}$ amounts to roughly 5.9 nT (0.25 Hz ^{1}H frequency).

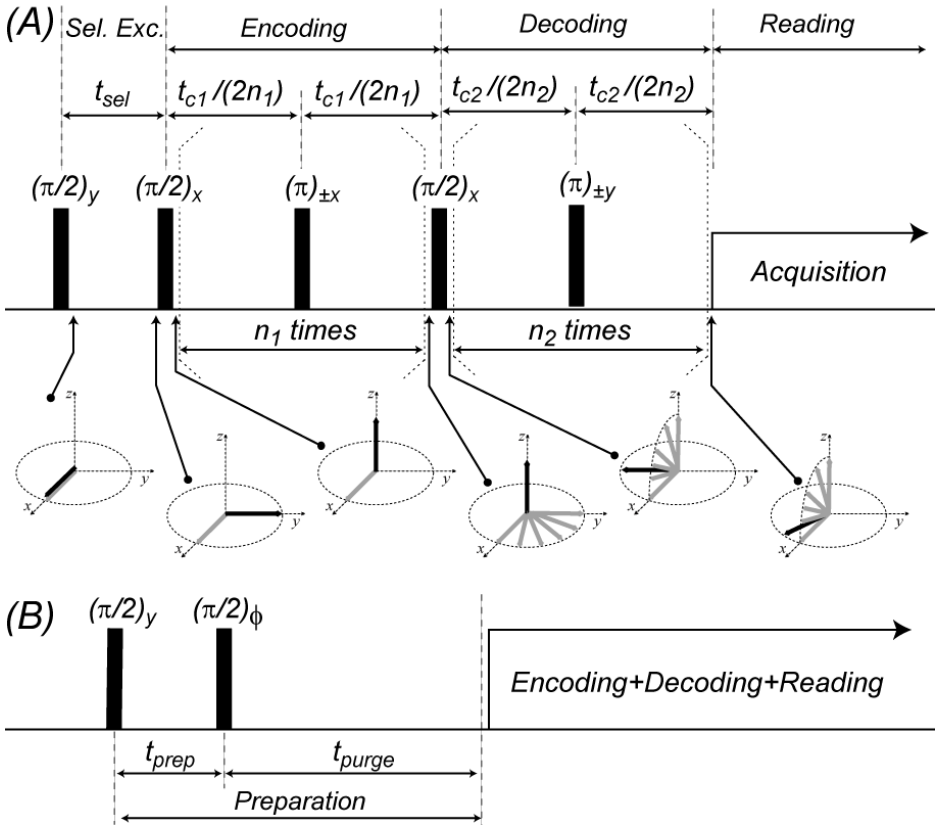

Fig. 2.1: (A) Pulse protocol for indirect detection of the sample magnetization. During the 'encoding' period, sample spins (indicated by gray arrows) evolve in the presence of the dipolar field due to the sensor. The gained phase depends on the position of the sample spin relative to the water droplet. A $\pi/2$ 'transition pulse' at the end of this period simultaneously excites water spins (black arrows) and generates a non-homogeneous distribution of sample magnetization along the z-axis. This induces a dipolar field on the sensor, which translates into a slow precession of the water nuclei. Trains of π-pulses with alternating phase during the 'encoding' and 'decoding' intervals are used to eliminate the effect of field inhomogeneities (or frequency offset). An even number of pulses has been assumed to simplify the drawing but this condition is unnecessary. Acquisition starts at the last echo point. Selective excitation of sample nuclear spins was

carried out using a pair of phase-shifted π/2-pulses; t_{sel} was chosen as ¼ the inverse of the frequency difference between the oil and water resonances (0.13 ms). (B) A 'preparation' interval preceding the pulse sequence in (A) is used to control the initial sample magnetization along the *z*-axis. The phase ϕ is chosen so that, irrespective of t_{prep}, sensor spins point along the +*z* direction after the second π/2-pulse; a purge period t_{purge} of 100 ms was used in all cases to eliminate remnant in-plane sample magnetization.

The presence of an additional external magnetic field acting on the water nuclei translates into a slow evolution of the water magnetization during t_{c2}. Notice that the synchronous inversion of the sample and sensor magnetization during this (and the former) time interval eliminates dephasing induced by field inhomogeneities but preserves the action of the dipolar field. The expected result is a slow precession of the sensor spins at the frequency of the sample dipolar field. Fig. 2.2 shows the spectrum of the signal recorded after t_{c2}. The oil peak – here kept as a reference for demonstration purposes – is due to in-plane magnetization originating from nuclei only weakly affected by the water dipolar field during the encoding period. After short time intervals, the water signal shows a 90-degree phase shift relative to the oil peak, a simple consequence of the phase difference introduced at time tc1 during excitation of the water nuclei. As the contact time t_{c2} increases, however, this phase shift progressively diminishes until the water peak becomes in phase with the oil peak at about 1.4 s. No significant changes are observed at later times; after 2 s of evolution, a low signal to noise ratio makes detection impractical.

These results are in good agreement with the model sketched above: taking 1.4 s as the time needed to induce a π/2-rotation of the water nuclei, the *effective* dipolar field due to the sample during the decoding period amounts to 0.17 Hz. This number is considerably smaller than the crude estimate indicated above (0.25 Hz) but the agreement

improves significantly if the various mechanisms of relaxation are taken into account. For example, when longitudinal and transverse relaxation times (identical for an isotropic liquid) are considered[21], a full numerical simulation of the spin dynamics in this system[22] yields an effective dipolar field of 0.19 Hz. Pulse imperfections during the sequence

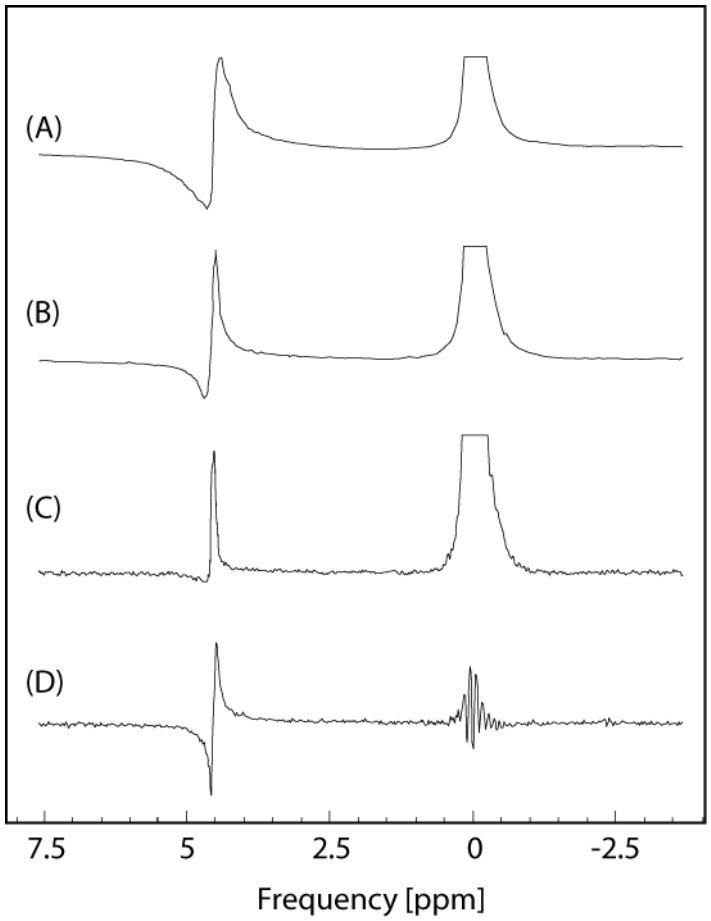

Fig. 2.2: Fourier transform of the signal detected after a variable decoding time; tc2 was set to 200 ms in (A), 700 ms in (B) and 1400 ms in (C). The evolution of the sensor spins in the presence of the sample dipolar field appears as a slow phase shift of the water peak. The phase of the oil resonance peak – shown truncated and used as a reference – remains undistorted. In all three cases a preparation time of only 5 □ s was used leaving both the oil and the water initial magnetization undistorted. A purge time of 100 ms was used; the number of scans was 16. The number of echoes n1 and n2 were 3 and 7, respectively. (D) Same as in (C) but with tprep chosen to saturate the sample spins (0.13 ms). In the absence of an external dipolar field, the water resonance peak exhibits no phase shift.

(particularly during the trains of π-rotations in the encoding and decoding periods) further decrease this value. Note that although a single inversion is necessary to eliminate the effect of field inhomogeneities (much stronger than the dipolar field to be measured), several π-pulses are preferred in practice. This is because damping of the measured signal due to self-diffusion can be lessened by decreasing the free evolution time between inversions, therefore improving the signal-to-noise ratio to a level compatible with our detection sensitivity. It is worth pointing out, nonetheless, that self-diffusion effects are not expected to considerably attenuate the (relevant) dipolar field neither during t_{c1} nor t_{c2}. Water self-diffusion is unimportant both during the encoding period (because the droplet dipolar field remains unaltered) and throughout the decoding time interval (because the oil dipolar field is fairly homogenous). On the other hand, oil exhibits a self-diffusion coefficient considerably smaller than that of water making diffusion effects rather negligible for the time scale and physical dimensions of the system under consideration.

The ability to indirectly detect the oil NMR signal by inspecting the water sensor is shown in Fig. 2.3. Here the pulse sequence is preceded by a preparation interval in which the oil magnetization is manipulated to modify the state prior to the encoding period. A 100 ms purge time between the preparation and encoding pulses was used to eliminate remnant in-plane oil magnetization. The phase of the 'transition' pulse at t_{c1} was changed by 180 degrees in even-numbered acquisitions to cancel the imaginary component of the water signal (see Fig. 1). The result is that the sensor signal will be non-zero only when an external dipolar field is present; further, the sign of the water peak will reflect the alignment (along the *z*-axis) of the sample nuclei inducing this field. In case 3a, the short preparation time used (5 μs) leaves the oil magnetization unchanged

and consequently, the water peak appears in-phase. Almost no signal is detected in case 3b, because the preparation time (0.13 ms) was chosen to saturate the oil spins; i.e., no dipolar field was acting on the droplet during t_{c2}. Finally, the water peak changes sign in case 3c reproducing the inversion of the sample magnetization during the preparation interval (t_{prep}=0.26 ms). Note that the signal amplitude is comparable to that of case 3a. This is consistent with the short overall increment of the sequence duration relative to the sample and sensor relaxation times (roughly 2 s).

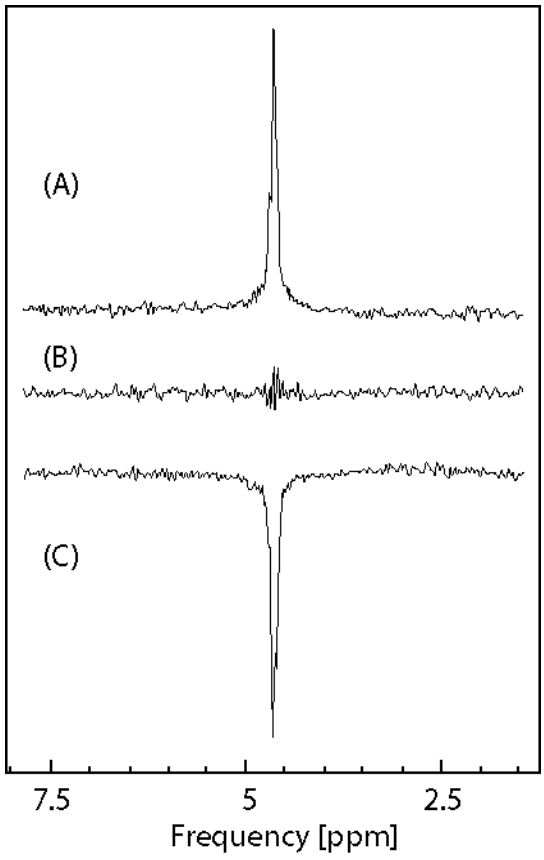

Fig. 2.3: When the phase of the 'transition pulse' (third π/2-pulse in Fig. 2.1A) changes 180 degrees in every scan, the dispersive component of the water signal is averaged out (after an even number of acquisitions). Therefore, the amplitude of the resulting absorptive sensor peak becomes proportional to the sample magnetization as set in the preparation period. In (A), the sample magnetization is left unchanged using t_{prep}=0.005 ms; it becomes zero in (B) setting t_{prep}=0.13 ms and is inverted in (C) with t_{prep}=0.26 ms. In all cases, t_{purge} was 100 ms and the total number of scans was 32. The number of echoes n_1 and n_2 were 3 and 7, respectively.

2.4 Discussion

Indirect detection of nuclear magnetic resonance as reported here could become a valuable strategy if the sensor is engineered to enable the use of detection methods more sensitive than standard Faraday induction. or example, detection of the nuclear polarization at the nanoscale has been demonstrated using electrical methods[23] and is currently investigated by several groups.[24] Further, Optical Faraday Rotation[25] and luminescence-based schemes[26,27] have been used to probe the nuclei contained in a semiconductor heterostructure[28] or in a single quantum dot.[29] In the present context, the high sensitivity common to these detection strategies could be exploited to locally probe an arbitrary sample (having non-zero nuclear spins) through a sensor optimized to provide the best possible signal. Clearly, various geometries are conceivable although a tip/sample configuration is particularly appealing and has been the subject of our recent study.[1]**Error! Bookmark not defined.** Because the size of the probed sample is comparable to the ize of the tip, a spatial resolution exceeding that attained by standard schemes could be possible. Dipolar Field Microscopy (DFM) – the name we have suggested for this strategy – could thus be used to reconstruct images as the tip scans the sample. Alternatively, it could be used to reconstruct a local high-resolution NMR spectrum if the preparation interval preceding the detection protocol (encoding and decoding periods) is sequentially incremented.

The results reported in this manuscript are insufficient to address the many technical questions associated with the practical implementation of DFM though they provide a reasonable starting point and a demonstration of the underlying physics. Notice that, in a sense, the absence of homonuclear decoupling during the preparation and

encoding periods – required when the sample or the sensor are solids – makes the analysis of this experiment perhaps more complex. This is because it is not evident whether non-linear effects due to internal demagnetizing fields in the sample and detector can be neglected during the spin evolution. It is not very difficult, however, to qualitatively demonstrate that this is indeed the case: In our setup, the field inhomogeneity (approximately 60 Hz FWHH) is tens of times larger than the magnitude of the inner demagnetizing fields (less than 1 Hz). The result is that the in-plane components of this field will be effectively averaged away; only the z-component of the inner demagnetizing field in the sample (sensor) must be considered during the encoding (decoding) time interval. A simple calculation demonstrates that this component is zero when the sample (sensor) magnetization lies along the xy-plane, which is practically the case during tc1 (tc2). A full numerical simulation that takes into account the spatial configuration in our system further supports this conclusion. These results[30] – not included here for brevity – indicate that the inner dipolar field will be weak even in the case in which the main magnetic field is perfectly homogeneous (due to the singular geometry of our experimental setup). A full account of these and other details is in preparation and will be published elsewhere.

From a more general perspective, an interesting feature of the proposed scheme is that the role played by the sample magnetization is merely to define the contact time necessary to modulate the sensor magnetization. Thus, as long as relaxation can be ignored, the detection sensitivity does not depend on the sample magnetization but only on our ability to pick-up the sensor signal (which, as mentioned, can be favorably engineered). These contrasts with standard Faraday detection: if S and F respectively

represent the signal-to-noise ratio obtained with standard inductive detection and the proposed method, S drops by half when the sample magnetization is reduced by the same amount. In the proposed scheme, however, one can double the contact time t_{c2} in which case F will remain unchanged. In other words, within the limits imposed by relaxation, it is possible to trade contact time in a single scan to gain a better signal-to-noise ratio. At the low temperatures required for DFM, this feature could prove beneficial in various applications, for example, to characterize dilute samples.

2.5 Acknowledgement

The authors gratefully acknowledge Phillip Stallworth for his valuable assistance during the experiments.

Chapter 3

Indirect detection of NMR via geometry-dependent dipolar fields, revisited

3.1 Abstract

We explore the dipolar interactions between two separate nuclear spin ensembles in a mixture containing oil and water. Here we expand initial to the case in which both systems have the shape of flat, stacked disks. We find that—in spite of the strong inhomogeneity of the coupling dipolar field—the signal encoded in one of the components can be made approximately proportional to the magnetization in the other. This allows us to use one of these systems as a ‘sensor’ to indirectly reconstruct the resonance spectrum or to determine the relaxation time of the ‘sample’ system. In the regime in which dipolar interactions are sufficiently strong, our method can be set to scale-up weaker signals in a non-linear fashion, which, potentially, could allow one to introduce contrast or to improve detection sensitivity of less magnetized samples.

3.2 Introduction

Because dipole – dipole interactions decay as the inverse cube of the inter-nuclear distance, dipolar effects between non-neighboring nuclei are usually deemed exceedingly small and therefore unimportant in most applications. During the past decade, however, several investigations made it clear that this argument must be handled very carefully[31,32,33]. The reason is that in the molecular ensemble present in all NMR experiments, the number of terms in the sum of all dipolar interactions with a given spin increases with the square of the distance to this spin. Dipolar couplings effective over macroscopic distances become therefore non-negligible when the sample magnetization is not isotropic, i.e., when contributions to the dipolar field at the center of a sphere surrounding the spin of interest do not exactly cancel. In most experiments to date, this is accomplished by inducing a magnetization grating through the application of a field gradient pulse at some stage of the NMR pulse sequence. This approach has been exploited extensively by the Warren group[18,34,15] and by Bowtell and collaborators [35,36,37] to develop a number of applications for either liquid-state NMR spectroscopy or medical imaging. The present study entails the investigation of the longrange dipolar interactions between two neighboring but separate spin ensembles, here in the form of an oil/water mixture. Unlike prior reports[38,39,15], our strategy makes use of the dipolar fields arising from the shape and relative location of each ensemble. A central goal in these studies is to control the dipolar coupling between the two spin ensembles so as to indirectly probe one of them (playing the role of an invisible sample) through its effect on the other

(operating as a sensor). This manuscript completes and expands preliminary results [40] by considering an array of a different geometry in which both oil and water phases have the shape of flat, consecutive disks with the main central axis aligned to the external magnetic field. We demonstrate that the sensor signal can be made approximately proportional to the sample magnetization making it possible to indirectly determine the sample resonance spectrum or relaxation time. The result is attractive because it proves that the sensor need not be immersed within the sample but can, instead, sit on its surface. Interestingly, the strength of the dipolar coupling between these two systems is insensitive to the absolute dimensions of the array. This leads us to envision a number of extensions of this or related schemes, this time to manipulate dipolar interactions between small, mesoscale systems.

3.2 Results and Discussion

The inset in Fig. 3.1 shows a picture of a setup similar to that used in our investigation. The system can be modeled as two (relatively) flat, stacked disks of distilled water (colored) and oil (Fluka DC 200) with their central axes aligned to the external magnetic field. In calculating the effect of the dipolar field of one system on the other, the presence of a dominant magnetic field B_0 makes it possible to neglect, as usual, all non-secular contributions to this field. Further, since water (‘sample’) and oil (‘sensor’) resonance frequencies differ by almost 5 ppm (1.8 kHz in our 9.4 T magnet), one can consider the combined system as heteronuclear and limit the contribution of the ‘sample’ dipolar field over the ‘sensor’ volume to the component parallel to B_0 (assumed along

the z-axis)[40] . Although obtaining a formula that describes the spatial dependence of this latter field is difficult, a numerical calculation is straightforward[41]. Close to the interface, the z-component of the dipolar field reaches a magnitude equal to $B_{spl}^{\max} = 5\mu_0 M_{spl}^{(0)} / (4\pi)$, where μ_0 is the vacuum magnetic permeability and $M_{spl}^{(0)}$ denotes the sample equilibrium magnetization. This amplitude decays monotonously over the sensor volume (assumed equivalent to that of the sample) to reach a value approximately 30% that of its maximum on the side of the sensor disk farthest away from the sample. At room temperature in a 9.4 T magnetic field, $B_{spl}^{\max}$ amounts to roughly 12 nT (0.5 Hz ^{1}H frequency).

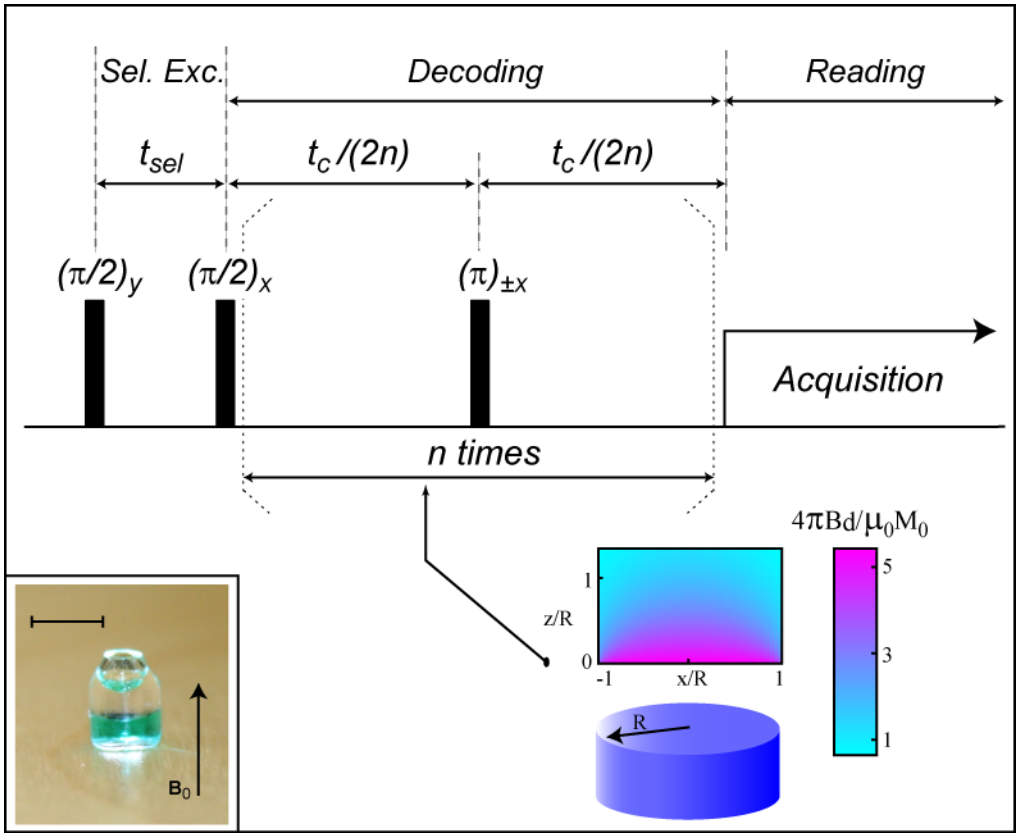

Fig. 3.1 Main: Water (sample) and oil (sensor) spin ensembles have the shape of comparable, flat disks stacked along the direction of the external static field B0. The pulse sequence utilized to probe the sample magnetization is shown on the top. After selective excitation, sensor spins evolve in the presence of the sample dipolar field for a variable 'contact time' t_c. Hard p-pulses of alternated phase are intercalated during this evolution to compensate for inhomogeneities of the main static field. The echo forming after t_c is finally acquired for inspection. Throughout the sequence, t_{sel} is kept fixed at a value equal to one fourth the inverse of the frequency shift between oil and water resonances. The drawing at the right lower corner displays the dipolar field induced by the sample magnetization on the sensor volume. The calculation assumes that the sample has a height h equal to the radius R. Note that the amplitude of the dipolar field on the sensor depends only on the geometry of the sensor/sample system (and therefore remains unchanged if all dimensions in the array are simultaneously scaled). Left lower corner: Photograph of an array similar to that used in the experiments. Sample and sensor occupy comparable volumes and have the shape of disks of diameter approximately equal to half the height. The scale bar corresponds to 3 mm. For clarity, water at the bottom of the container was artificially colored by admixture of a green dye.

Fig. 3.2 displays the Fourier transform of the signal obtained during the 'reading period' for different contact times t_c. Successive spectra exhibit a slow but clear phase evolution that can be interpreted as the slow modulation introduced in the signal (Hahn echo) due to the cumulative effect of the sample dipolar field on the sensor. Notice that in the pulse sequence of Fig. 3.1, field inhomogeneities or frequency offsets are cancelled through the application of π pulses during the 'decoding' period; long-range dipolar fields, however, remain effective due to the simultaneous inversion of sample and sensor spins. No phase change was observed in the measured signal each time the sample magnetization was saturated prior to the application of the pulse sequence, therefore confirming that the presence of the sample dipolar field is crucial. The magnitude of this field as measured from the observed phase evolution amounts to 0.35 Hz, in qualitative agreement with that expected from an average of the dipolar field over the sensor volume

(see Fig. 3.1). The effect of the sample dipolar field on the evolution of the sensor magnetization can be made more explicit by adding consecutive acquisitions while alternating both the receiver phase and initial direction of the sample magnetization . In the pulse sequence of Fig. 3.1, the latter is accomplished by increasing in 180-degree steps the phase of the second π/2-pulse during the selective sensor excitation. With this procedure, the sensor signal (after an even number of scans) becomes

$$S_{snr} \propto \int_{V_{snr}} dr^3 M_{snr}^{(0)} \sin\left(\gamma_{snr} t_{c2} B_{spl}^{(z)}\right) \tag{3.1}$$

where γ_{snr} denotes the sensor gyromagnetic ratio, $B_{spl}^{(z)}$ is the (secular) dipolar field due to the sample, $M_{snr}^{(0)}$ is the equilibrium sensor magnetization and the integral is calculated over the sensor volume. Experimental results illustrating our ability to measure the sample dipolar field—and, therefore, its local magnetization—are shown in Fig. 3.2 g for a fixed contact time t_c chosen, so that $\gamma_{snr} t_{c2} \left\langle B_{spl}^{(z)} \right\rangle < \pi/2$ (the brackets are used to indicate average over the sensor volume). A simple protocol (similar to that of Fig. 3.3) was used here to scale the sample magnetization (and, therefore, the dipolar field) prior to the application of the sequence of Fig. 3.1 The sensor signal is observed to evolve as expected, with amplitude approximately proportional to (the sine of) the sample magnetization. The response ‘saturates’ in the region of strongest sample dipolar field although the observed dependence can be ‘relinearized’ by shortening the ‘decoding’ time t_c (therefore forcing $\gamma_{snr} t_{c2} \left\langle B_{spl}^{(z)} \right\rangle < \pi/2$ even in the case of maximum sample magnetization). Depending on the ratio between the contact time and the sensor relaxation time this may (or may not) result in a smaller signal amplitude (vide infra).

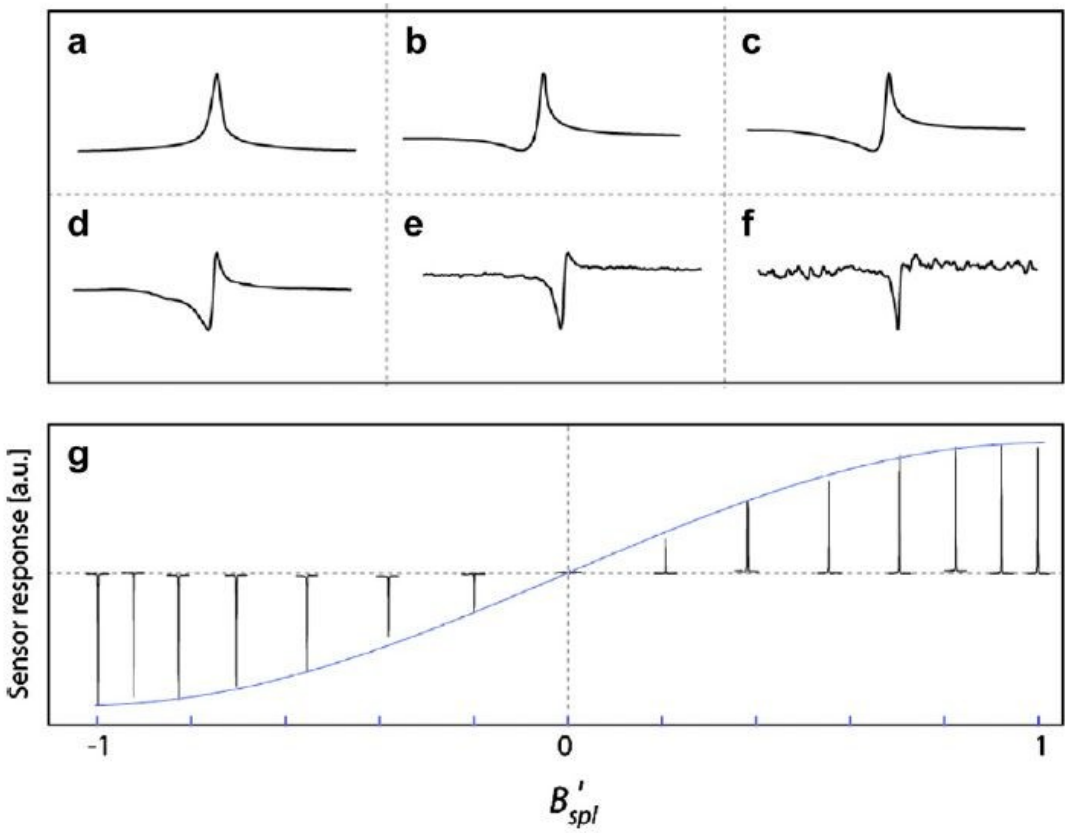

Fig. 3.2 Fourier transform of the sensor signal (oil) obtained after a variable contact time using the pulse sequence of Fig. 3.1 The sample dipolar field induces a slow precession of the sensor magnetization observable through the progressive phase change of the echo. From top to bottom, the contact time was (a) 145 ms, (b) 550 ms, (c) 750 ms, (d) 1000 ms, (e) 1250 ms, (f) 1600 ms. The average field on the sensor—approximately 0.35 Hz—is strong enough in this case to induce a 180-degree phase shift of the sensor signal. The spectral bandwidth from (a) to (c) is 2.5 kHz. (g) 'Subtraction-mode' sensor signal at t_c = 0.8 s as a function of the sample dipolar field. A preparation protocol similar to that of Fig. 3.3 was used to vary the sample magnetization and, with it, the magnitude of the relative dipolar field B'_{spl} acting on the sensor. In agreement with Eq. (3.3), the sensor displays a sinusoidal response of the type , here shown as a solid line for comparison.

Dipolar couplings between the sample and sensor can be used not only to probe the sample magnetization but also to indirectly determine some of its basic NMR parameters. For example, indirect measurement of the sample T_1 via the sensor becomes straightforward with the use of a simple preparation protocol as shown in Fig. 3.3 Notice

that diffusion and relaxation effects (of both the sample and the sensor) during the ‘decoding’ period remain approximately constant throughout the process and, therefore, do not hinder an accurate measurement. The same principle can be extended to indirectly determine the sample resonance spectrum. In our experiment, this is accomplished by modifying the preparation protocol of Fig. 3.3a to probe in a ‘point-by-point’ fashion the in-plane evolution of the sample magnetization after selective excitation. Fig. 3.3c shows the resulting evolution of the sensor signal: Fourier transform along this time axis leads to a _1.8 kHz-shifted sample resonance peak in agreement with the measured chemical shift of the sample (water) relative to the sensor (oil) resonance frequency.

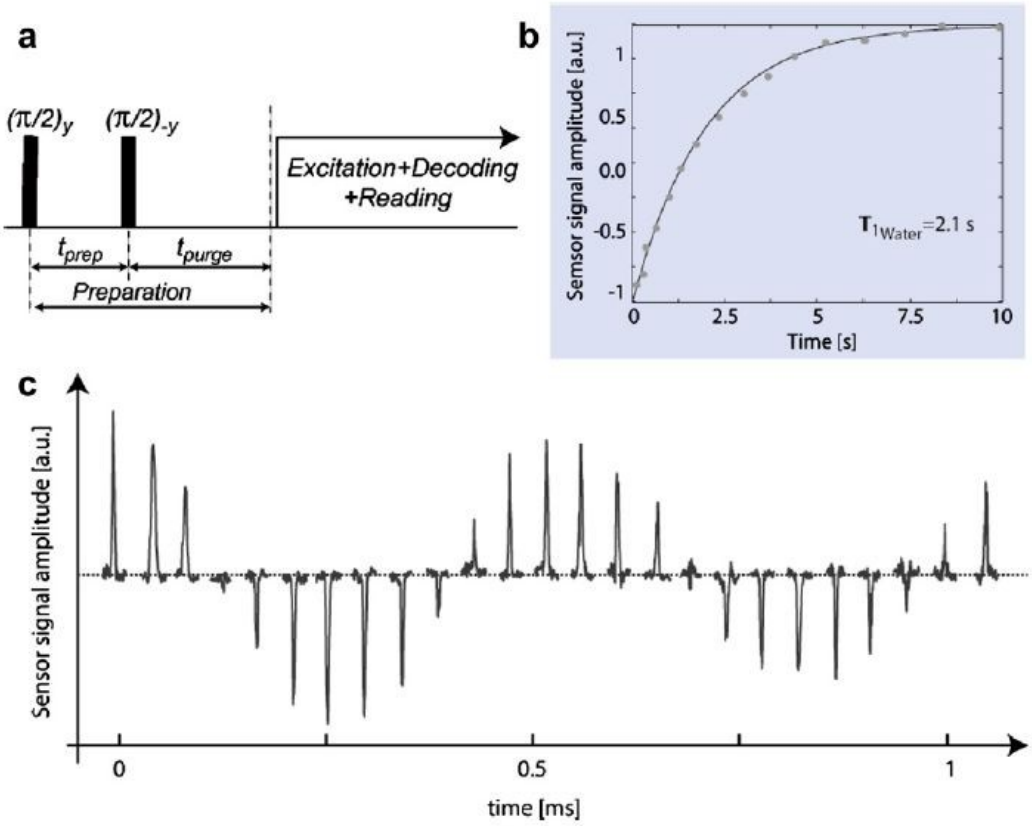

Fig. 3.3 (a), (b) Indirect determination of the sample relaxation time via the dipolar field on the sensor. The pulse sequence of Fig. 3.1 was preceded by a simple inversion-recovery protocol followed by a short purging time. Selective inversion of the sample spins was carried out by two consecutive π /2-pulses spaced by half the period corresponding to the oil-water frequency difference. The sample relaxation time was 2.1 s in good agreement with the value measured by direct observation. (c) Point-by-point determination of the sample resonance spectrum by observation of the sensor signal. A preparation protocol similar to that shown in (a) but with a variable inter-pulse spacing was applied to monitor the in-plane evolution of the sample magnetization. The contact time t_c was 0.5 s

A facet of the scheme introduced here that is worth exploring in some detail is the effect of relaxation on the amplitude of the signal encoded in the sensor. Shown in Fig. 3.4 is the evolution of the Fourier-transformed FID as a function of the contact time t_c. As before (see Fig. 3.2g), subsequent acquisitions of the sensor magnetization were co-added while simultaneously alternating the detector phase and the initial orientation of the sample magnetization. For contact times much shorter than the inverse of the dipolar field (expressed in frequency units), the peak amplitude tends to zero, as expected. At later times, Eq. (3.3) predicts a sinusoidal growth with its first maximum occurring at a time $t_c \cong (\pi/2)\left(\gamma_{snr}\left\langle B_{spl}^{(z)}\right\rangle\right)^{-1}$ (approximately 0.8 s). In practice, however, the maximum signal is observed at much shorter times (~0.2 s), when the gain arising from a greater phase change of the sensor magnetization is not overshadowed by transverse and longitudinal relaxation of both sample and sensor spins. Qualitatively, the effect of relaxation on the signal amplitude can be taken into account by introducing a time dependence on the sensor (and sample) magnetizations. Eq. (3.1) then writes

$$S_{snr}(t_c) \propto \int_{V_{snr}} dr^3 M_{snr}^{(0)} \exp(-t_c/T_{snr}) \sin\left(\int_0^{t_c} dt\, \gamma_{snr} B_{spl}^{(0)} f(t)\right) \tag{3.2}$$

where T_{snr} represents the transverse relaxation time of the sensor and $f(t)$ is a function that takes into account the decay of the sample dipolar field during the 'decoding' period. This decay can be induced either by longitudinal sample relaxation or the repeated application of π-pulses affected by rf inhomogeneity. Fig. 3.4 shows the result for the case $f(t) = \exp(-t/T_{spl})$ with T_{spl} denoting the longitudinal relaxation time of the sample. Shown for comparison is also the curve obtained through a numerical simulation; both curves qualitatively reproduce the observed behavior although overall agreement (particularly at short times) is moderate. We presently ignore the causes but we speculate that this is due to artifacts in the selective excitation of the sensor magnetization due to modest shimming and rf homogeneity.

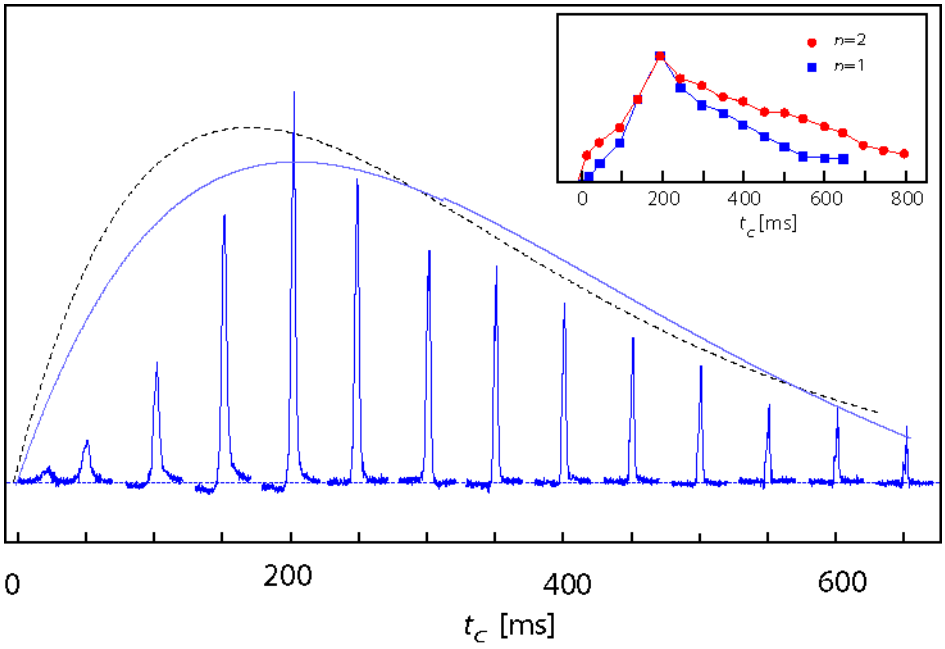

Fig. 3.4 Signal amplitude as a function of the contact time. In-phase spectra were obtained by pairing subsequent FID's while synchronously alternating the sign of the initial sample magnetization (see text). After a rapid initial growth, the amplitude diminishes exponentially. The dashed curve corresponds to Eq. (3.2) with

$f(t) = \exp(-t/T_{spl})$ whereas the continuous curve indicates the result of a numerical simulation. Only one inversion pulse was applied during t_c. **Inset:** Decay of the signal due to diffusion can be mitigated by incrementing the number of inversion pulses. Shown for comparison are the results using one and two inversion pulses during t_c.

At long contact times, the observed behavior is dominated by the transverse relaxation rate of the sensor. In the presence of a relatively strong static field inhomogeneity such as that of our setup, spin diffusion does contribute to induce a faster decay. As expected, the inset in Fig. 3.4 shows that this effect can be partly mitigated by increasing the number of inversion pulses (until the cumulative action of rf inhomogeneity on the sample dipolar field precludes further improvement). We will soon make use of this feature to explore different scenarios in which the ratio between the contact time t_c and the sensor decoherence time T_{snr} is varied.

Assuming that the sensor has been chosen to provide the best possible signal-to-noise ratio, Eq. (3.2) indicates that our ability to boost detection sensitivity of the sample signal depends critically on the product of the time $t_c^{opt} \cong (\pi/2)\left(\gamma_{snr}\left\langle B_{spl}^{(z)}\right\rangle\right)^{-1}$ (necessary to induce maximum modulation of the sensor magnetization) and its transverse relaxation rate $(T_{snr})^{-1}$: full sensor sensitivity will be attainable when $t_c^{opt} / T_{snr} \approx 0.3$ or smaller but will be correspondingly reduced in other cases. For instance, in Fig. 3.4 the highest signal amplitude at 200 ms amounts to only a small fraction (~10%) of the theoretical maximum (which, in the absence of relaxation, corresponds to the 'full' water signal and occurs at the 'optimum' contact time $t_c^{opt} \approx 0.8$). Although indirect detection of the sample signal as shown here becomes obviously impractical in the presented setting, the use of

the sensor may be favored in situations where stronger dipolar couplings make the contact time significantly shorter or when detection sensitivity in the sensor largely surpasses that possible in the sample[1,40]. Note that in this latter scenario, a contact time much shorter than the 'optimum' value may still make indirect detection comparatively favorable. A regime in which the contact time is much shorter than the spin decoherence time can be exploited so as to determine the sample magnetization via the time needed to induce in the sensor a predetermined phase change (as opposed to detecting the phase evolution over a fixed contact time). In this 'inverse' mode, the contact time required in a sample with half the magnetization would last approximately twice as long but the overall phase change in the sensor signal would remain unaltered. The advantage is that, under the right conditions, a weaker sample magnetization can be probed almost without compromising detection sensitivity. To render this idea more formal, we write

$$t_c = \frac{\varphi}{\gamma_{snr}\left\langle B_{spl}^{(z)}\right\rangle} \tag{3.3}$$

indicating that for every local magnetization $\left\langle B_{spl}^{(z)}\right\rangle$ the contact time t_c is chosen so as to induce in the sensor a phase change ϕ ($\leq \pi/2$). If, for simplicity, we assume[42] $T_{snr} << T_{spl}$, we use Formula (3.2) (with $f(t)=1$) to write

$$S_{snr}\left(B_{spl}^{'}\right) \propto M_{snr}^{(0)} \sin\varphi \exp\left(-\frac{t_c^{ref}}{T_{snr}B_{spl}^{'}}\right) \tag{3.4}$$

Here $B_{spl}^{'} = \left\langle B_{spl}^{(z)}\right\rangle / \left\langle B_{ref}^{(z)}\right\rangle$ represents the local magnetic field relative to that in a reference (which could be a section of the sample with a strong magnetization) and t_c^{ref}

indicates the time needed to induce in the latter a phase change ϕ. Fig. (3.5) displays the normalized sensor signal $S'_{snr} = S_{snr}\left(B'_{spl}\right)/S_{snr}(1)$ as a function of the relative, local dipolar field for different values of t_c^{ref} and T_{snr}; in this drawing the diagonal corresponds to the usual, inductive detection where the signal-to-noise ratio scales linearly with the amplitude of the sample magnetization. As long as the contact time remains shorter than the sensor (and sample) relaxation times, the curves indicate a slower loss of sensitivity relative to that typical in standard detection methods. In our experiment, we reach this regime by choosing t_c^{ref} =300 ms ($\phi \sim \pi/3$) and by applying a total of six π-pulses during the contact time (which allows us to increase T_{snr} to ~700 ms). This strategy fails when a longer t_c^{ref} (i.e., a greater phase change ϕ) is necessary to increase the absolute signal amplitude (see Formula (3.4)) or when the interpulse spacing in the CPMG train is long (resulting in a lower T_{snr}).

3.3 Summary

In summary, this manuscript has explored the dipolar interactions between two separate, macroscopic nuclear spin ensembles having the shape of stacked, collinear cylinders. We find that the sensor signal roughly scales with the local sample magnetization thus making it possible to indirectly determine the resonance spectrum or relaxation rate in one of them via its effect on the other. When the decoherence time of the sensor magnetization is sufficiently long (or when the sample/sensor dipolar coupling is sufficiently strong), our strategy can be altered to increase detection sensitivity only at the expense of extending the contact time. In an array where the sensor is free to move

over the surface of a larger, extended sample, this scheme could be used to advantage to explore areas of the sample that are weakly magnetized or as a way to introduce (image) contrast. It is worth stressing at last that the strength of the coupling between the spin ensembles depends only on the magnetization and relative geometry, which makes this strategy appealing as the absolute dimensions of the components diminish. Possibly the most exciting extension of these ideas entails the control of dipolar interactions in solids. At the low temperatures required for this implementation, high-sensitivity detection methods could be exploited to indirectly probe the sample magnetization with a spatial resolution defined by the size of the sensor [21]. Work along these lines is currently under way in our laboratory.

3.4 Acknowledgement

The authors are indebted to Dr. Boris Itin for valuable assistance with some of the experiments reported here. This research was supported by NSF through a CAREER program. W.D. and C.A.M. are members of the New York Structural Biology Center (NYSBC), a STAR center supported by the New York State Office of Science, Technology and Academic Research. NMR resources at the NYSBC are supported in part by the National Institutes of Health (Grant P41 GM66354).

Chapter 4

Detection of Long-Range Dipole－Dipole Interactions between Nuclear Spins in Distant Solids

4.1 Abstract

Prior work demonstrated that a given nuclear spin subset in a fluid can be monitored via the NMR signal from another, non-chemically bonded subset, even if within a separate container. Here we report an extension of these results to the case in which both ‘sample’ and ‘sensor’ spin systems are solids. For the present demonstration, we use the ^{71}Ga signal from GaAs to detect the nuclear dipolar field induced by proton spins from an adjacent organic sample. Multipulse decoupling sequences are used to minimize homo- and heteronuclear couplings within the ‘sensor’ while preserving the long-range interaction with the proton field. Potential applications of this result are briefly discussed.

4.2 Introduction

Although the effects of the average nuclear spin magnetization on individual spins are ignored in the traditional description of NMR, early observations in ^{3}He showed that long-range dipolar fields can have a substantial influence on the nuclear spin evolution[12]. With the advent of more sensitive NMR spectrometers, subsequent work found unmistakable signatures of the so-called ‘demagnetizing field’ in the spectra of densely protonated fluids at room temperature. In particular, studies led by the Warren group and by Bowtell and coworkers demonstrated that longrange dipolar interactions in fluids can be exploited to indirectly probe the NMR signal of a ‘sample’ spin species not chemically bonded to the ‘sensor’ spin[14], even when both ‘sample’ and ‘sensor’ spins occupy separate (but neighboring) containers[15]. In all these experiments, gradient fields are used to break the symmetry of the sample polarization and thus induce a non-vanishing dipolar field, the strength and range of which can be controlled by altering the duration of the gradient pulse. On the other hand, long-range dipolar interactions can also be introduced geometrically by asymmetric sample/sensor arrangement[40]. These couplings, in turn, can be exploited to probe the sample magnetization and relaxation time or even to indirectly reconstruct the sample spectrum[43]. This possibility serves as the platform for recent proposals[19,1] aimed at overcoming the limitations of induction-based NMR detection, the idea being that a careful selection of the shape, size and composition of the ‘sensor’ spins can result in a significant improvement of the ultimate detection sensitivity.

With no applied field gradients, the results we present in this manuscript fall in this last category: for the present demonstration we prepared a system in which a thin disk of GaAs sits on a sample of powdered Adamantane firmly pressed to the bottom of a container. With ^{71}Ga nuclei playing the role of 'sensor' spins, the goal of this experiment was to detect the proton 'long-range' field – which, naturally, scales linearly with the 'sample' magnetization – through its effect on the evolution of the 'sensor' spins. We note that the strategy we explore here is quite general in the sense that it does not depend on the particular material compounds chosen for this demonstration, but on the contrary can be extended to other systems (at least conceptually, so long as each individual spin subset is addressed selectively). On the other hand, selection of the sensor material was guided by the assumption that small amounts of 'sample' spins could be *indirectly* detected if known high-sensitivity techniques (alternative to Faraday induction) are used to probe the nuclear polarization of small GaAs probes. Later in the manuscript we will return to this important point.

On a final, more general note, we mention that the idea of relying on a carefully chosen sensor system dipolarly coupled to a set of unknown, target spins is also at the core of the most recent proposals aimed at increasing detection sensitivity. In addition to those already mentioned[19,1], another example is the work of Taylor et al.[44] describing the use of NV centers in diamond to sense the random dipolar fields induced by neighboring spins. Also worth mentioning is the Letter by Cappellaro et al.[45] where the signal of a target spin is amplified by dipolarly coupling it to an ensemble of sensor spins.

4.3 Experiment

A diagram of our experimental setup is shown in Fig. 4.1a: a 3 mm-diameter, 3 mm-thick disk of pressed, powdered Adamantane ($C_{10}H_{16}$, Aldrich) sits at the bottom of a teflon container, underneath a thinner (0.3 mm) disk of semi-insulating GaAs (AXT Semiconductors) cut to the same diameter. The system is immersed in a 9.4 T magnetic field and at room temperature. Although obtaining a formula that describes the spatial dependence of the proton long-range field is difficult, a numerical calculation is straightforward[43] and has been included in Fig. 4.1b. Near the surface, the z-component of this field reaches a magnitude equal to $B_d = 5\mu_0 M_0/(4\pi)$, where M_0 denotes the proton magnetization and μ_0 is the vacuum permeability. This value varies smoothly over the GaAs volume having a dispersion of only $\pm$ 10%. For the conditions of our experiment, B_d amounts to roughly 7 nT.

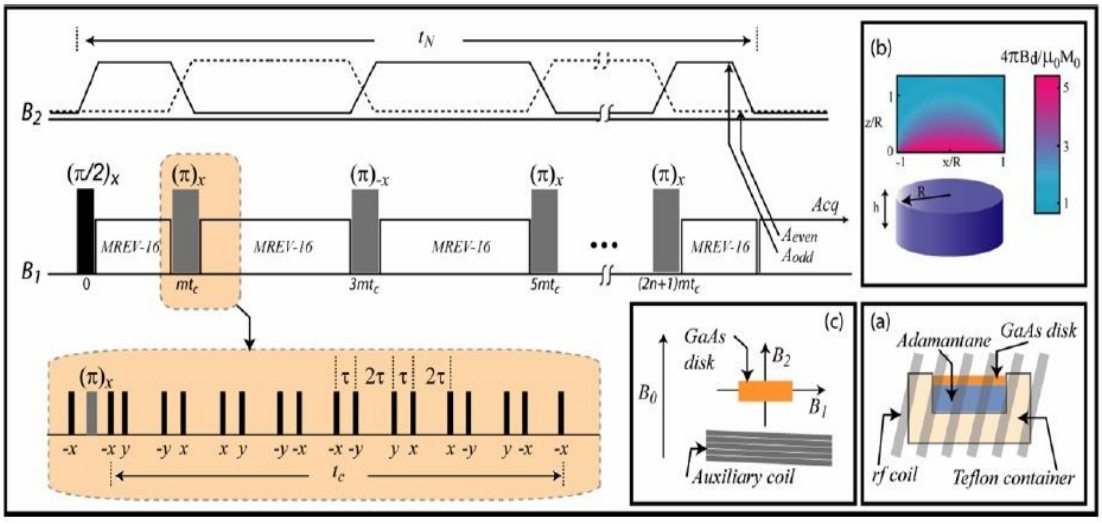

Fig.4.1 *(Inset A)* Schematics of the sensor/field geometry. *(Inset B)* Calculated nuclear magnetic field for a disk of radius R and thickness $h = R$. The magnetic field profile is shown as a function of the relative horizontal distance y/R from the disk center and height z/R from the disk surface. Values of the dipolar field B_d are expressed in units of

the disk magnetization M_0; μ_0 denotes the vacuum permeability. *(Inset C)* An auxiliary coil replaces the sample in test measurements that rely on a calibrated magnetic field. *(Main)* Schematic of the detection protocol. After excitation of the GaAs sensor spins, a sequence that intercalates MREV-16 cycles with periodic inversions suppresses ^{71}Ga homo- and heteronuclear dipolar couplings between nuclear spins within the sensor material. To preserve the effect of the external field on the ^{71}Ga evolution, synchronous modulation was introduced either by periodically switching off the auxiliary coil or by inverting the proton magnetization through phase-alternating p-pulses (not shown). Comparison of the signals A_{odd}, A_{even} after modulation of the 'unknown' field B_2 during complementary intervals between inversions allows for a direct measurement of the effective field amplitude (see text). Unless otherwise noted, all pulses in the diagram are $\pi/2$-rotations having the shown relative phase; t_c is the MREV-16 cycle time and m is an integer.

While signatures of comparable magnetic fields are easily observable in fluids[43], indirect detection in solids is obviously complicated by the presence of a much stronger internal dipolar field (of order 300 μT in GaAs). Given the huge disparity between these two fields – and, as explained below, the resulting practical difficulties inherent to our experiment – we first conducted preparatory measurements in which the amplitude of the observed field was artificially increased. For this purpose we used the auxiliary setup sketched in Fig. 1c: here, the GaAs disk sits in the vicinity of a solenoid whose central axis is parallel to that of the main field B_0. The current – and therefore the field B_2 produced by the solenoid – can be amplitude modulated by external means. The effective magnitude of this field as a function of the solenoid current was determined by observing the proton spin resonance in a fluid organic sample (where several-second-long coherence times allow for detection down to sub-nanotesla fields). Resonant excitation of the 'sensor' spins and control of their temporal evolution was carried out with a homebuilt double resonance probe whose low-frequency channel was tuned at the ^{71}Ga

NMR frequency (122 MHz). The second, high-frequency channel was used to simultaneously manipulate proton spins when present (see below). To reduce the effect of homonuclear dipolar interactions during the evolution time of the ^{71}Ga spins we employed MREV-16[46,47]. A train of π-pulses spaced at integer numbers of MREV-16 cycles was introduced to counter additional dephasing due to heteronuclear interactions and field inhomogeneities[48]. That the net effect of this combined pulse sequence is the one desired can be seen from the fact that the leading-order, average Hamiltonian at the end of each MREV-16 cycle reduces to the (scaled) chemical shift and hetero-dipolar contributions. π-pulses, therefore, must be effective against both terms so long as the time interval between successive inversions is kept shorter than the inverse of the spin diffusion rate.

With this pulse sequence minimizing homo- and heteronuclear dipolar couplings, the value of a magnetic field other than B_0 acting on the sensor was measured from the change of the sensor-spin precession frequency (a standard practice in Larmor magnetometry[49]). In the present case, a subtle variation of the Larmor frequency following excitation appears as a phase shift of the NMR signal recorded after a pre-determined evolution time t_N. Static fields have no effect on the average spin evolution because, as is well known, the net phase gained during equal intervals before and after the application of a π-pulse is zero. This is clearly not the case, however, when the direction of the sensed field is inverted after a π-pulse or, in general, if the amplitude of the field is altered with every inversion.

A direct determination of the phase shift – and therefore of the 'unknown' field – is obtained by comparing the amplitudes of the NMR signals A_{odd}, A_{even} from two successive measurements: during the first one, the sensed field B_2 is maximum at odd intervals between π-pulses, whereas B_2 is stronger at even-numbered intervals during the second measurement. For a given field, the phase shift θ can be calculated from the relative amplitude of the combined signal $A_r = (A_{odd} - A_{even})/(A_{odd} + A_{even}) = \sin\theta$.

We remind the reader that removal of homonuclear dipolar interactions through multipulse sequences comes at the price of an effectively slower spin precession frequency about the sensed magnetic field. The 'scaling factor' characterizing this effect is equal to 1/3 in an *ideal* MREV-16 sequence where the rf pulses have negligible duration[6,44] . Although in practice this condition is rarely attained, ^{31}P measurements in phosphoric acid – a fluid we used as a reference – showed that the scaling factor remains close to the ideal value if only the 'rf-free' time is taken into account when computing the total evolution time after excitation.

As shown in Fig. 4.2, the same seems to be the case for GaAs: comparison between observed and predicted values of the phase shift (assuming scaling equal to 1/3) shows reasonable agreement at times $t_N \leq 40\,ms$ within the range of applied field amplitudes B_2 . This is not the case at longer times were unavoidable imperfections progressively accumulate to dominate the spin evolution. The finite duration of the pulse cycle certainly represents an inherent limitation that results in the incomplete suppression

of the dipolar interactions[45] . Note, however, that other sources such as rf inhomogeneities or rf phase transients often play the dominant role. The direct result is an effectively shorter coherence time and thus a reduced sensitivity to magnetic fields.

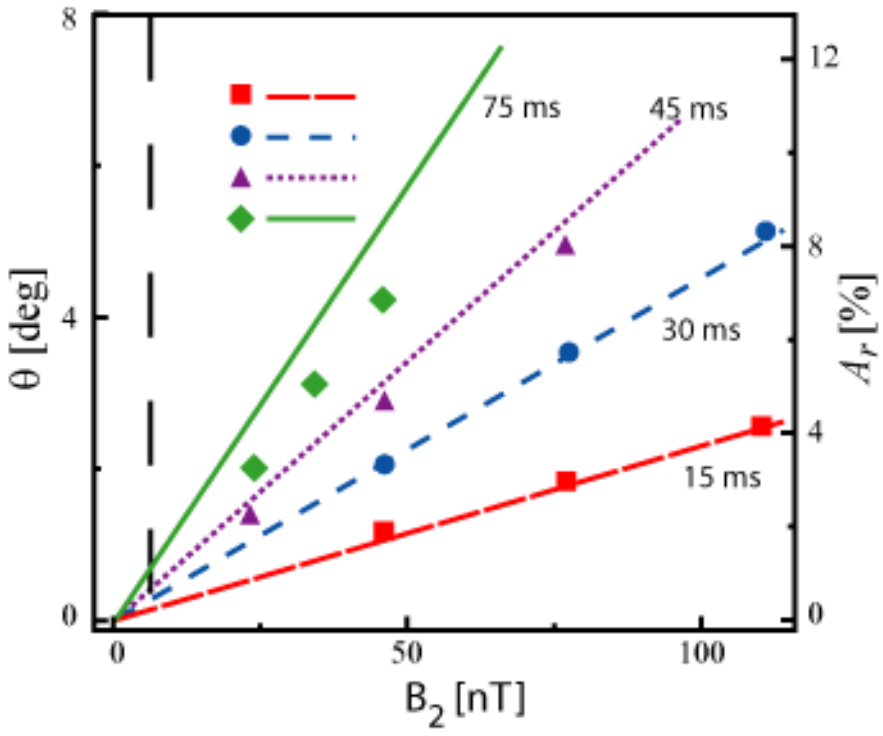

Fig. 4.2 ^{71}Ga phase shifts as a function of B_2 for different decoupling times. Lines indicate expected shifts for an 'effective' scaling factor equal to 1/3 (see text). The vertical dashed line indicates the approximate value of B_2 in the experiment of Fig. 4.3 The duration of the ^{71}Ga $\pi/2$-pulses was 3 μs, the interpulse separation in MREV-16 was 8 μs and the total cycle time was 240 μs; π-pulses were applied every two MREV-16 cycles.

The extension of these preparatory results to probe the nuclear spin dipolar field of an adjacent 'sample' is summarized in Fig. 4.3: For this experiment, the auxiliary coil has been de-activated and the GaAs sensor sits on powdered Adamantane as

described above. Note that at □ 7 nT, the ‘long-range’ sample dipolar field lies slightly above our practical limit of detection (□ 1 nT, see below). Synchronous modulation of the magnetic field due to protons in Adamantane was carried out via a train of inversion pulses tuned at 400 MHz, the proton spin resonance.

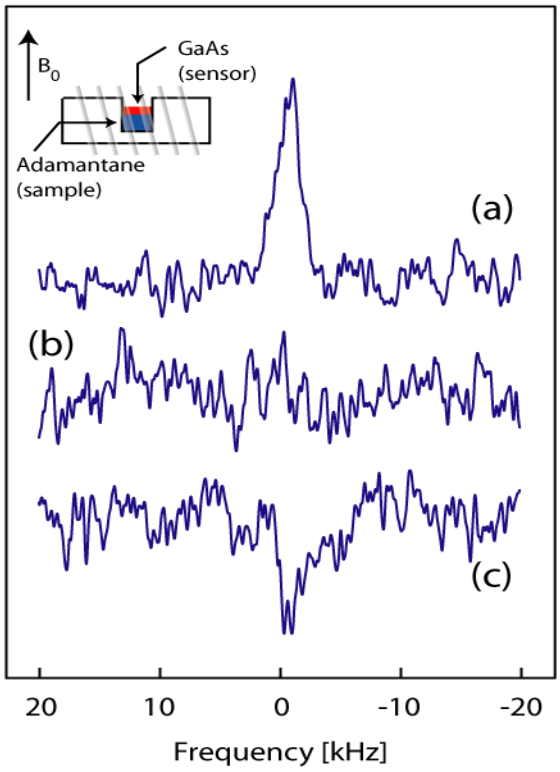

Fig. 4.3 **(Inset)** Protons from a 3 mm diameter, 3 mm thick disk of pressed, powdered Adamantane induce a magnetic field of _7 nT over the GaAs disk volume. Shown in **(a)** is the GaAs signal in the presence of full ‘sample’ magnetization at room temperature. As expected, this signal disappears in **(b)** or changes sign in **(c)** when proton spins are either saturated or inverted prior to detection. Signals were obtained after 2000 scans; the decoupling time was 50 ms and the interpulse separation $_s$ was 8 μs. The duration of the π-pulses was 6 μs for ^{71}Ga and 9 μs for ^{1}H. All other conditions as in Fig. 4.2

Each trace in Fig. 4.3 is the result of 2000 scans; to prevent overheating of the probe and sample, a one minute delay between successive FIDs was necessary making for a total experiment time of about one day per run. A simple preparation protocol consisting of a pulse of variable length followed by a 500 μs -purging interval allowed us to alter the initial proton magnetization and, with it, the field acting on the GaAs disk. The first two traces respectively show that the sensor signal due to the presence of the total proton magnetic field (a) disappears if the sample magnetization is saturated prior to detection (b). By the same token, the sign change observed in case (c) reflects the inversion of the proton magnetization preceding the sensing protocol. From the signal amplitudes, we estimate the proton dipolar field at $\sqcup$ 5 nT in reasonable agreement with the predicted value.

4.4 Discussion

A critical parameter in the experiment of Fig. 4.3 is t_N, i.e., the time during which 'sensor' spins are allowed to probe the 'sample' long-range field: inexorable decoherence at longer contact times soon outweighs the gain resulting from greater accumulated phase shifts. A straightforward calculation demonstrates that the optimum signal is attained at a time coincident with the transverse relaxation time[40] . We note, however, that in the present experiment this is not strictly the case. This is because, in multipulse sequences such as MREV-16, the (average) sensor spin precession about the probed magnetic field often degenerates into 'spinlocked' magnetization along an effective rf field direction[50]. Well documented though poorly investigated, this effect is intimately related to pulse

imperfections and could not be completely avoided in the experiments reported herein. This is shown in Fig. 4.4 where the phase shift observed after a given evolution time at a fixed (coil-induced) magnetic field of 100 nT is compared against the amplitude of the GaAs signal (similar measurements using the proton field are prevented given the inherent low signal-to noise ratio). Though a significant fraction of the initial ^{71}Ga magnetization is still present after t_N = 50 ms (the decoupling time used in the experiment of Fig. 4.3), the observed phase shift effectively saturates at later times signaling the beginning of a smooth transition to a 'spin-locked' state. Note that, in the absence of B_2, no significant phase shift is present in the GaAs signal (Fig. 4.4b) suggesting that the 'spin-locked' field is pointing along a direction coincident with that of the magnetization immediately after excitation.

It is worth pointing out that we observed similar effects also when using other, more sophisticated decoupling sequences such as BR-24 [51] and SME-16 [52]. This observation is in agreement with a prior report[47] in which identical pulse sequences were used to decouple ^{29}Si spins in solid silicon. Notably, however, the effective decoupling time attained here is far from that reported in Ref. 47, approaching 25 s for natural silicon – 4.7% abundant – and up to 3 s for a 98%-isotopically-enriched sample. The causes for this huge difference are not clear at the moment although, at least in part, may stem from poorly removed heteronuclear couplings with ^{69}Ga and ^{75}As spins (60% and 100% abundant respectively). For example, we noticed that the separation between π pulses (spaced every two MREV-16 cycles) proved to be an important parameter: longer lasting coherences were obtained by shortening the inter-π-pulse separation, but frequent

inversion also proved to have a deleterious, 'spin-locked' effect. On the other hand, test measurements revealed small but non-negligible phase instabilities throughout the multipulse sequence (apparently, inherent to our spectrometer) that, overall, further contribute to shorten the effective decoupling time. Finally, we note that uncompensated imperfections present in the train of (phase-alternating) π-pulses modulating the proton long-range field lead to progressive attenuation of the 'sample' magnetization. As a result of these (and some other) practical limitations, we roughly set our present limit of detection at $\sqcup$ 1 nT for a one day experiment.

In addition to demonstrating – to the best of our knowledge, for the first time – that long-range dipolar interactions can be detected and manipulated in physically-separate, solid-state spin systems, the results presented here could find extensions worth exploring. In particular, potential applications as a detection strategy alternative to Faraday induction seem not out of the question[1]. In this context, an advantage of geometry-induced dipolar couplings is that the strength of the resulting interaction depends only on the *relative* dimensions of the component spin subsets. Conceptually, therefore, the results reported herein can be thought of as 'scaleinvariant', meaning that, in principle, an experiment that utilizes a smaller 'sensor' coupled to a correspondingly smaller 'sample' would leave identical imprint on the sensor signal. Semiconductors in general (and GaAs in particular) have the potential to play a useful role along this path. We note that, owing to the comparatively strong hyperfine interaction present in this kind of materials, several schemes[53,54] have been demonstrated in the recent past that allow for the detection of nuclear spins over volumes down to

$\sim 10^{-4}\,\mu m^3$. We stress that none of these (or other[28]) schemes is applicable to organic materials in general (where the hyperfine coupling is strongly suppressed) providing a compelling motivation for indirect detection. It is worth pointing out that extensions of the presented strategy are possible in which the sensor interacts with only the neighboring fraction of an extended sample[1]. Because in this case the spatial discrimination is dictated by the size of the 'sensor' used, we speculate that a strategy similar to that presented here could be applicable in a geometry in which a properly engineered semiconductor 'tip' scans the surface of an extended, organic sample at low temperatures. Finally, we mention that the addition of a simple protocol of the type $(\pi/2 - t_{evol} - \pi/2)_{sample}$ prior to 'sensor' manipulation would allow for a 'point-by-point' detection of the local 'sample' spectrum or relaxation time as the evolution interval t_{evol} is sequentially incremented. The latter has already been demonstrated for dipolarly-coupled fluids[43] and may find an extension in a 'scanning tip' geometry to introduce either relaxation- or spectroscopic based contrast when reconstructing an image.

4.5 Conclusion

We have demonstrated an 'all-solid' detection of the long-range dipolar field of a densely protonated solid by monitoring the evolution of ^{71}Ga nuclear spins in GaAs. The sign and magnitude of the proton-induced magnetic field – and thus of the 'sample' proton magnetization – result from a simple strategy that makes the observed signal proportional to the subtle frequency change resulting from the presence

of the proton field. Imperfections in the multi-pulse sequence used to reduce homo- and hetero-nuclear dipolar interactions between 'sensor' spins preclude the observation of magnetic fields smaller than □ 1 nT (although prior results in similar systems reported by other groups lead us to believe there is substantial room for improvement [48,55]). When examined as a detection strategy, it seems possible to imagine extensions of the presented scheme that exploit the proven ability to detect small numbers of nuclear spins in semiconductors. Because the strength of the long-range couplings – and, therefore, the amplitude of the effect they cause in the sensor signal – remains unchanged as the system dimensions diminish, potential applications to NMR microscopy seem worth exploring in detail. Similar to methods such as force-detected magnetic resonance[56], low temperatures may be necessary to reach the highest sensitivity[1]. Nonetheless, the added ability to reconstruct local NMR sample spectra could prove rewarding.

4.6 Acknowledgement

We are indebted to Prof. J. Reimer for his valuable comments. This research was supported by NSF through a CAREER award. C.A.M. acknowledges the Research Corporation for its support through the Cottrell Scholar program.

Chapter 5

Helicity-independent Optical Pumping of Nuclear Magnetization in Bulk CdTe

5.1 Abstract

We report on the observation of optically pumped nuclear spin polarization in samples of CdTe at high magnetic field using ^{125}Te NMR. We find strong enhancement both in bulk material as well as in a MBE grown, 2 μ thick epilayer. Contrary to prior results, however, we observe that the magnitude and orientation of the nuclear spin alignment is independent of laser helicity. Further, we find that after its onset at sub-bandgap energies, the nuclear polarization rapidly increases to reach ~3% and remains virtually unchanged as higher energies are scanned. Comparison with additional data from a semi-insulating GaAs crystal points to a polarization mechanism different from that typically dominant, possibly driven by surface spin-dependent recombination.

5.2 Overview

The interplay between electron and nuclear spins in semiconductors and the optical enhancement of nuclear polarization are topics of continuing interest due to the promise of spin-based quantum computation and sensitivity-enhanced magnetic resonance. While, in general, most recent studies have focused on 'optically pumped' spins in confined structures, a string of observations point to a still incomplete understanding of the dynamics of nuclear polarization in bulk systems. For example, measurements of the nuclear polarization in GaAs derived from the asymmetries of quadrupolar-split NMR lines seem to suggest that both localized and delocalized electrons collaborate in the optical pumping (OP) process.[57] And while the Fermi contact contribution to the hyperfine coupling was assumed dominant in direct semiconductors, the role played by the dipolar component still remains controversial.[58,59] Another example is the recent work of Hayes and collaborators[60,61] who have shed light on some of the intricacies in the electro-optical processes leading to nuclear OP in GaAs.

The results we present herein focus on the dynamics of nuclear polarization in bulk CdTe. We use ^{125}Te NMR to directly monitor the optically-enhanced nuclear polarization at high magnetic field both in a single crystal and in a MBE-grown CdTe epilayer. We find an intriguing dependence of the induced nuclear polarization with photon energy and helicity that cannot be explained within the traditional theoretical framework, thus pointing to alternate polarization pathways. Although it is not possible at this time to rule out other mechanisms, our observations seem consistent with spin-dependent recombination via surface shallow donors.

To more clearly introduce our results we recall that in direct-bandgap semiconductors, optical pumping of nuclear spins is typically described as a transfer process, in which the angular momentum of circularly polarized light cascades down to electrons and then to nuclear spins. The first step is made possible by the optical selection rules present in this type of materials:[62] With the z-axis representing the direction of illumination, the corresponding projection of the electron spin immediately after light excitation is predicted to have a value $S_z = \pm 0.25$, depending on the helicity of the beam. Under steady-state conditions and assuming the Faraday geometry (i.e., illumination parallel to the external magnetic field), the resulting, quasi-equilibrium spin magnetization is given by[63]

$$S_{eq} = S_z / \left(1 + \tau / T_{1e}\right) + S_0 / \left(1 + T_{1e} / \tau\right) \tag{5.1}$$

where T_{1e} and τ indicate the electron spin relaxation and recombination times, respectively. $S_0 = -(1/2)\tanh\left(g^* \mu_B B_0 / 2k_B T\right)$ is the thermal spin alignment of electrons with g-factor g^* in a magnetic field B_0 at temperature T; μ_B and k_B denote as usual the Bohr magneton and Boltzmann constant.

The transfer of angular momentum to the nuclear spin system takes place via the hyperfine interaction between nuclei and conduction electrons; holes, on the other hand, typically play a less important role because the π-like character of the hole wavefunction guarantees a negligible density at the nuclear site (and thus a strongly reduced hyperfine coupling). Within this framework, enhancement of nuclear magnetization is observed when the electron-nuclear relaxation time T_{1H} is much shorter than the nuclear spin-lattice time T_{1L}, *and* the steady state electron polarization differs from the thermal value.

If we ignore inhomogeneities in the spatial distribution, the predicted quasi-stationary value of nuclear polarization is given by[64]

$$I_{OP} = I_0 + f\,\frac{I(I+1)}{S(S+1)}\,\frac{1}{(1+\tau/T_{1e})}(S_z - S_0) \tag{5.2}$$

with I_0 denoting the average nuclear spin projection along the field direction in thermal equilibrium and $f \equiv 1/(1+T_{1H}/T_{1L})$ indicating a 'leaking factor' due to nuclear spin relaxation with the lattice.

5.3 Experimental setup and samples

To directly monitor the optically-enhanced nuclear polarization in our samples, we relied on a setup similar to that described previously.[65] High-field, variable-temperature experiments were carried out using a 9.4 T NMR magnet and a continuous flow cryostat with optical access. The sample was in good thermal contact with a sapphire wafer to facilitate heat dissipation, and a Cernox sensor (additional to the built-in, cryostat RTD) was placed in its proximity to provide more reliable temperature readout. Laser illumination was, as usual, parallel to the direction of the magnetic field (and perpendicular to the sample surface); the addition of an optical expander allowed us to vary the beam diameter from ~3 to 0.5 mm. To excite and detect nuclear spins we used a home-made, two-channel probe head; cryogenic capacitors allowed us to tune and match the rf circuit down to 4 K and over a broad range of frequencies. We studied three samples: the first one was a semi-insulating CdTe single crystal from University Wafers (resistivity > 10^9 Ω cm, surface orientation [111]). The second one was a 2 μ thick, MBE-grown CdTe epilayer (surface orientation [100]) on a GaAs substrate; a thin ZnSe

layer (1 nm) was intercalated between the CdTe film and the substrate to improve the film quality.[66] Finally, we used a semi-insulating GaAs single crystal as a control (350 μ thick, surface orientation [100], resistivity greater than 10^7 Ω cm, American Crystal Technologies).

Detection of nuclear polarization was preceded by the known protocol $SAT\text{-}\tau_L\text{-}\tau_D\text{-}\pi/2$ where τ_L and τ_D indicate illumination and dark intervals respectively, and $\pi/2$ represents the excitation rf pulse. Saturation (*SAT)* prior to illumination was carried out via a string of resonant $\pi/2$ pulses. ^{125}Te NMR spectra for both the CdTe single crystal and film at sub-bandgap energies are shown in Fig. 5.1 The beam diameter was ~1 mm and the laser power was 300 mW. Consistent with the long relaxation times found in CdTe (of order ~10 min at room temperature and exceeding several hours below 80 K), no signal was observed in the dark. On the other hand, strong enhancements that do not depend on the beam polarization were found in both samples when the laser was on. Notably, the signal amplitude in the film was almost identical to that observed in the crystal implying that polarized nuclei lie within less than 2 μ from the surface. Using the room-temperature signal from the 5x5x0.35 mm^3 CdTe crystal as a reference and assuming an effective volume of illumination of ~1x1x2x10^{-3} mm^3, we estimate a nuclear polarization of order 3%.

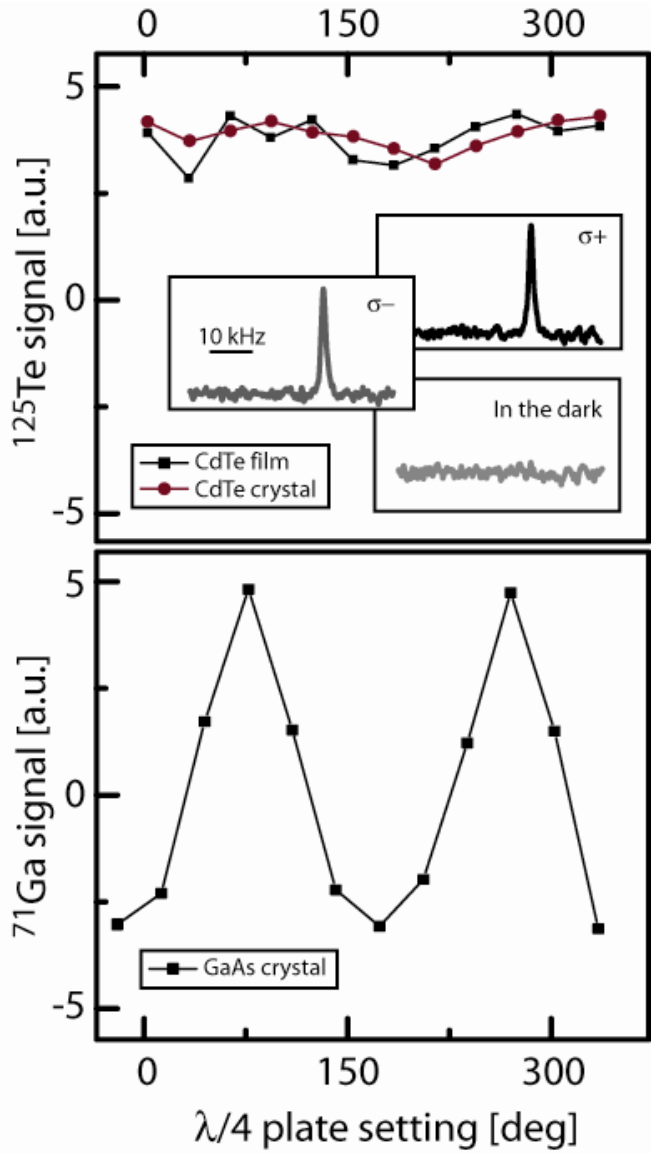

Fig. 5.1: (a) ^{125}Te optically-enhanced signal as a function of the light helicity (expressed via the quarter-wave plate setting). Squares (■) and circles (●) indicate the NMR signal from film and crystal respectively. Note that the relative amplitude is close to unity implying that the signal originates from superficial nuclei. The inserts show actual (crystal) spectra in the absence of illumination and for exciting light of opposite helicity (FWHM~2kHz). The magnetic field is 9.4 T, the temperature is 5 K, the laser power 300 mW and the beam diameter 1-2 mm. The illumination wavelength was 800 nm, τ_D =10s and τ_L=300 s (τ_L=1200 s in the inserts). (b) Corresponding results in a control crystal of semi-insulating GaAs under similar experimental conditions (light excitation at 827 nm). To facilitate comparison, the absolute amplitude of the ^{71}Ga NMR signal was multiplied by a factor two.

In spite of several attempts, practical limitations did not allow us to determine the sign of the induced alignment relative to thermal polarization: in the absence of illumination, the above-mentioned nuclear relaxation times make comparison *after* OP exceedingly difficult. On the other hand, comparison with the signal from partially-relaxed nuclear spins after the system cool-down but *before* optical excitation was prevented by our failure to detect crystal nuclei in a single scan. (Note in this regard that given the relative dilution of ^{125}Te and small crystal size several scans are necessary to attain reasonable signal-to-noise ratio at room temperature).

5.4 Results and discussions

The response to light helicity observed in our CdTe samples differs from that seen in our control GaAs crystal where, in agreement to well-known results, signal inversion takes place when passing from right- to left-circularly polarized illumination. More importantly, our results differ from those reported previously in a CdTe crystal subject to similar conditions[67]: Though no inversion was present, this latter case showed a significant change between signals induced by light of different helicity. Further, when plotted as a function of photon energy, the signal amplitude was observed to peak slightly below the bandgap to sharply decay to a lower plateau at higher energies (a behavior somewhat reminiscent of that observed in GaAs[65]). As shown in Fig. 5.2, our samples exhibit a different dependence: the NMR signal does reach a maximum at sub-bandgap energies but then it remains virtually unchanged as higher photon energies are probed (note in this regard the broad energy range reaching 1.77 eV or 700 nm).

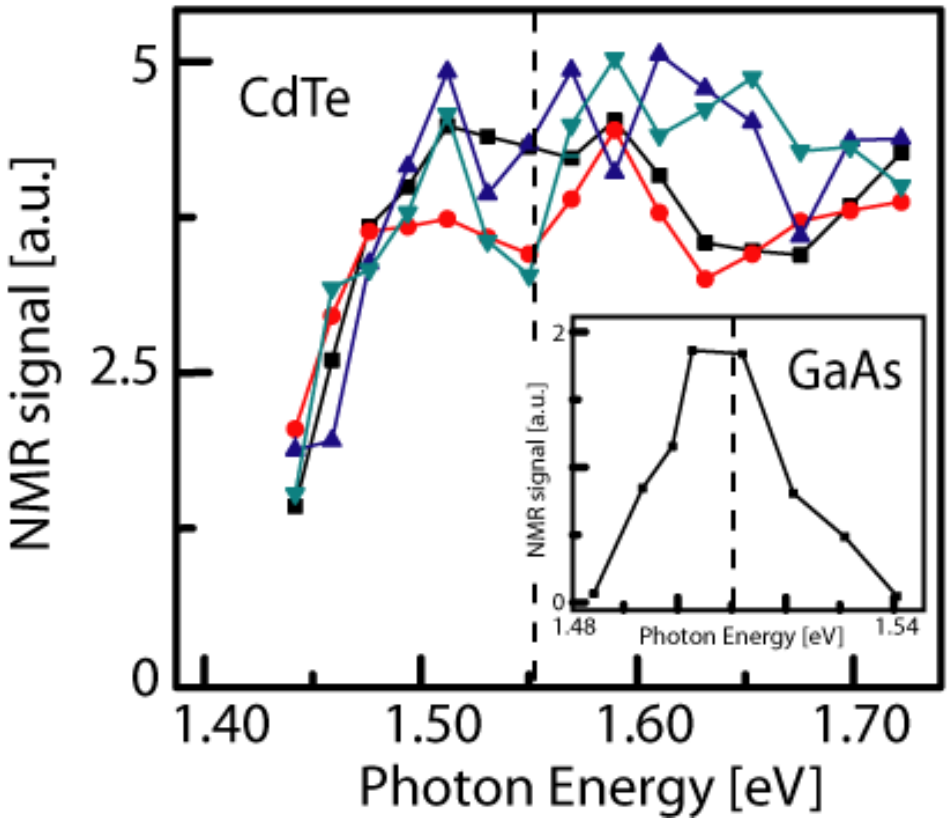

Fig. 5.2: (Main) ^{125}Te NMR signal amplitude as a function of the photon energy. Squares (■) and circles (●) indicate the crystal signal for left- (σ-) and right- (σ+) circularly polarized light while upright (▲) and inverted (▼) triangles provide identical information for the film. Experimental parameters as listed in Fig. 5.1 The dashed line indicates the bandgap energy at this temperature as determined from transmission measurements in our CdTe crystal. This value is in excellent agreement with that reported in the literature.[71] (Insert) Energy dependence for our control GaAs crystal under right-circularly polarized illumination.

Given the disparities pointed above, we made every effort to ensure the absence of systematic errors in our experiments; a particular concern was inadvertent laser heating, a parameter difficult to monitor and known to have non-negligible effects in OPNMR.[68] While results in our control GaAs sample suggest that our experiments are exempt from this problem, reassuring evidence is presented in Fig. 5.3: similar to observations in GaAs,

we find a linear increase of the observed signal with light intensity and a typical exponential growth with illumination time. More importantly, when plotted as a function of increasing lattice temperature, we observe a fast polarization decay that renders the NMR signal virtually unobservable above 20 K. (In passing, we note that no signal from the thin-film sample in the dark exceeded noise levels *at any temperature* further demonstrating the large magnitude of the enhancement). Remarkably, the decay rate is as fast as that found in GaAs, a somewhat unexpected observation given the longer lattice relaxation times T_{1L} of non-quadrupolar nuclear systems (all relevant spin isotopes in CdTe have spin ½).

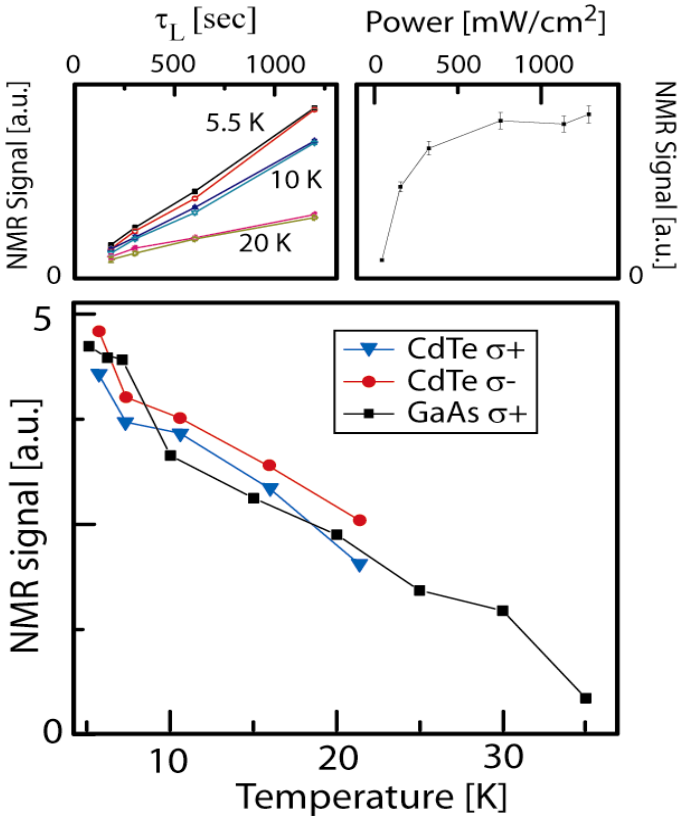

Fig. 5.3: ^{125}Te NMR signal amplitude as a function of illumination time τ_L, laser power density and temperature. For comparison, the last figure includes (scaled) ^{71}Ga results in our control GaAs sample. Experimental conditions as listed in Fig. 5.1

Though free excitons may participate in the process of nuclear spin polarization[57,65,67], shallow impurities and lattice defects are typically assumed to play a dominant role[69]: carrier localization by lattice imperfections leads to locally-enhanced hyperfine couplings and thus to efficient alignment of neighboring nuclei. Electron traps thus operate as nucleation centers of polarization, which, in turn, spreads throughout the crystal via spin 'flip-flops', a mechanism described in the OP master equation by a diffusion-like term.[70] As shown in Fig. 5.2, the observation of strong, sub-bandgap signal points to lattice imperfections driving the nuclear polarization process in our CdTe samples. Whether such imperfections are interstitial or substitutional impurities, vacancies, antisites, dislocations (or other types of defects) still remain to be determined. Some insight on the nature of these lattice imperfections is provided by the photoluminescence (PL) spectra shown in Fig. 5.4. Both CdTe samples show strong band-edge emission at 77 K but, unlike the crystal, the CdTe film shows virtually no deep level PL, which allows us to exclude this type of defect from those relevant to the OP process. Further, the main emission peak is slightly asymmetric toward higher energies, indicative of coexisting 'bound exciton' and 'free-to-bound' recombination (involving a trapped electron or hole and a free carrier).

With the intention to further characterize these nucleation centers, we also monitored the optically-enhanced NMR spectra at short pumping times. The importance of this strategy has been recently demonstrated by Hayes and collaborators, who observed strong light-induced hyperfine shifts in the NMR spectrum of semi-insulating GaAs.[61] Resulting from the hyperfine interaction of localized electrons with neighboring nuclei, these shifts depend on light helicity and are more notable at short illumination

times (before spin diffusion spreads the nuclear polarization farther away from the trapping centers).

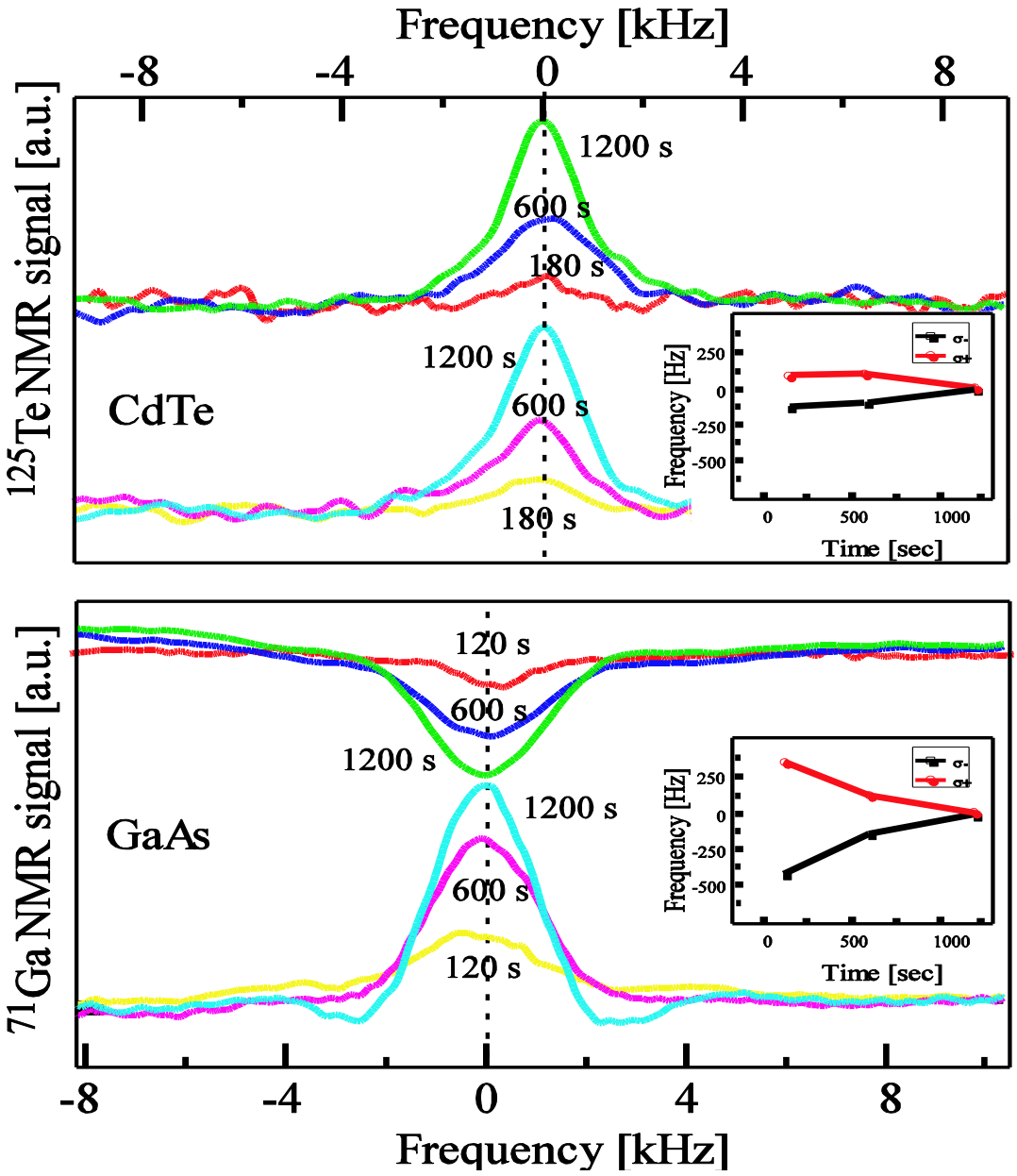

Fig. 5.4: Optically-pumped NMR spectra in (a) our CdTe crystal and (b) the GaAs control sample for different illumination times τ_L. Clear, helicity-dependent Knight shifts observable at short τ_L in GaAs are absent in CdTe. Spectra have been shifted for clarity. The temperature is 5 K, the laser power is 300 mW, the ^{125}Te and ^{71}Ga central frequencies at 9.4 T are ν_{Te}=126.022 MHz and ν_{Ga}=121.965 MHz, respectively. The illumination wavelength is 800 nm for CdTe and 827 nm for GaAs.

Fig. 5.5 shows results obtained in the CdTe crystal and our control GaAs sample: at τ_L=120 s we observe clear, helicity-dependent frequency shifts in GaAs, which progressively decay to virtually disappear at τ_L=1200 s in qualitative agreement with the results of Ref. 61. On the other hand, the CdTe NMR spectra do not visibly change with illumination time or light helicity. In a model where the nuclear polarization process is driven by localized electrons, this result may seem disconcerting. ^{71}Ga and ^{125}Te have comparable hyperfine couplings A_H (of order 50 μeV[69,72]) and, thus one would expect similar Knight shifts in both systems. (Note that the five-times-lower natural abundance of ^{125}Te as compared to ^{71}Ga is expected to serve only as a scaling factor, without altering the magnitude of the NMR shift).

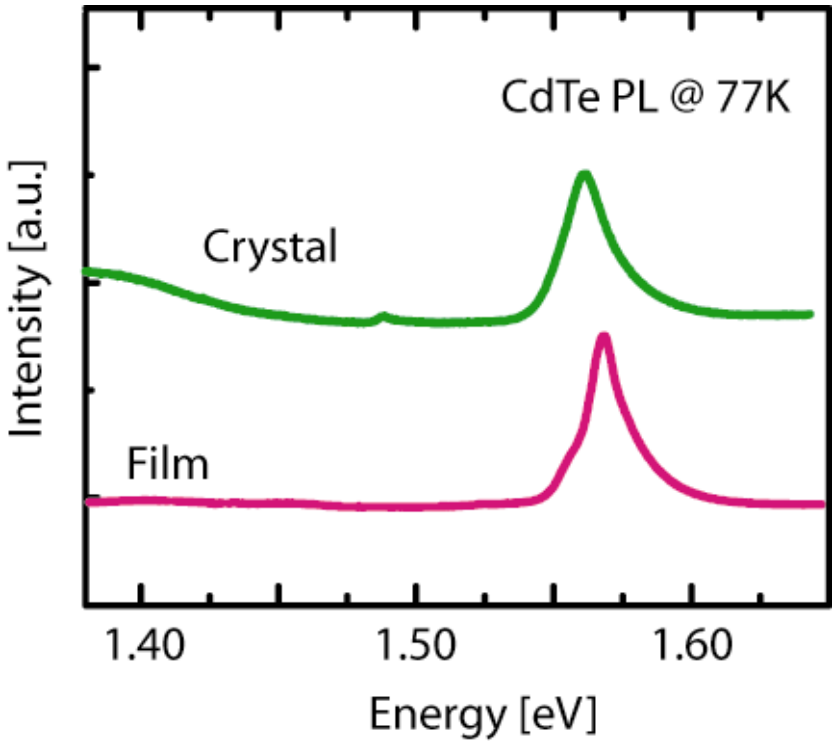

Fig. 5.5: Photoluminescence spectra from (a) the CdTe crystal and (b) the CdTe film at 77 K and zero magnetic field. The excitation wavelength is 1.77 eV (700 nm). Observe in both cases the tail toward higher energies. Deep level emission (around 1.4 eV) is only present in the CdTe crystal.

The idea that similar hyperfine couplings lead to comparable shifts is only granted if the function describing the spatial distribution of the trapped electron is also comparable: this is because the position-dependent Knight field $B_e(r) \sim k_e A_H \exp(r/a_0)$ decreases rapidly with increasing distance r to the trap.[69] The scale governing this decay is a_0, the excitonic Bohr radius, found to be only 6.8 nm in CdTe, almost half the value in GaAs (12.0 nm).[73] The latter has the important consequence that only a small number of nuclear spins close to a lattice defect will experience a substantial Knight field, or equivalently, that the illumination time required to observe an NMR shift becomes even shorter, a condition in conflict with the sensitivity of our experiment.

The behavior found in Figs. 5.1 and 5.2 is, perhaps, more intriguing: if for simplicity we ignore the *nuclear* thermal polarization I_0, Formula (2) demands that the observed OP signal be proportional to S_z-S_0, i.e. proportional to the difference between the expectation values of the electron spin *immediately* after light excitation and in thermal equilibrium. For an effective Landé factor $g^* \sim 1.64$ valid in bulk CdTe[74], a magnetic field of 9.4 T and a temperature of 5 K, we obtain $|S_0| \approx 0.38$. Therefore, the expected fractional change of the NMR signal upon reversal of the excitation beam helicity has magnitude $\left|I_{OP}^{+} - I_{OP}^{-}\right| \Big/ \left|I_{OP}^{+} + I_{OP}^{-}\right| = \left|S_z^{+} - S_z^{-}\right| \Big/ \left|2S_0\right| \approx 70\ \%$, in strong disagreement with our observations.

This last result points to nuclear spin polarization pathways different from those found in other systems. The nature of this alternate mechanism is unclear at this time but we speculate that the observed behavior originates from strong spin-dependent recombination (SDR). First observed by Lepine in pure silicon[75], we recall that SDR

alludes to a process in which excess electrons and holes recombine via paramagnetic impurities. When a conduction electron is captured by a paramagnetic center, the electron and center spins form intermediate singlet or triplet states.[76] The former has lower energy than the latter, a condition that makes singlet states considerably more localized and, more importantly, more prone to induce exciton recombination. Further, because the total angular momentum is conserved during optical transitions, singlet electrons with a particular angular momentum projection recombine preferentially if holes have a well-defined alignment.[59] The result of this process is, therefore, the selective polarization of the electron trapped at a donor.

In a SDR-dominated OPNMR experiment—where the nuclear spin polarization derives from selective recombination at shallow donors—helicity-independent signals can be expected when free carriers spin-relax *before* they recombine. The latter seems to be a *reasonable* assumption in the present case: as a matter of fact, holes are known to relax much faster than electrons in bulk, zincblende semiconductors owing to their stronger spin-orbit coupling. And while it is true that the electron spin lifetime may exceed the recombination time in certain systems, *n*-type doping (absent in our samples) is mandatory for excess carriers to spin exchange.[77] More importantly, time resolved optical measurements in CdTe epilayers very similar to the one used here[78] find $T_{1e}/\tau \sim 0.3$ at room temperature (sample labeled Y3 in Ref. 78) further confirming the idea that the nuclear polarization is helicity-insensitive simply because the optical imprint on the exciton spin is lost before it can be transferred to the nuclei. On a final note, we

mention that $T_{1e} < \tau$ is a sufficient *but not necessary* condition for helicity-independent nuclear signals, as other, more subtle scenarios with $T_{1e} = \tau$ are conceivable as well.

In Lepine's paper[75], it was shown that SDR in silicon is not homogeneously distributed over the sample volume but rather restricted to the surface (where the capture cross section is enhanced via charge-induced changes in the surface potential[75]). The observation that above 1.50 eV the ^{125}Te NMR signal is insensitive to excitation energy (Fig. 2) is consistent with a surface-confined, SDR-driven OP because, once photons exceed a threshold energy, the same number of centers remains active regardless the excitation wavelength. As discussed above, this is not the case in semi-insulating GaAs (Fig. 2), where the amplitude of the nuclear spin signal has been shown to correlate well with the (wavelength-dependent) absorption coefficient (and therefore with the excitation volume).[60,79]

If confirmed, the spontaneous confinement of enhanced nuclear polarization near the surface of CdTe could find interesting applications. For example, Tycko pointed that routinely used polarization-transfer schemes could be exploited to enhance the NMR signal of an organic thin film overlaid on a semiconductor substrate. The so-called 'spectroscopic barrier' precluding efficient transfer from systems of quadrupolar nuclei (e.g., GaAs) is absent in CdTe making this material a convenient choice. Note in particular that our estimate of the film nuclear polarization (3%) presumes homogeneous distribution over the 2 μ thickness; obviously, greater alignment must be present if only a thinner, superficial section is effectively pumped.

5.5 Conclusion

In conclusion, we have observed strong optical enhancement of nuclear polarization in bulk CdTe, both in a commercially available single crystal and in 2 μ thick, MBE-grown film. Comparison with measurements on a bulk semi-insulating GaAs sample subjected to virtually identical conditions exposes intriguing differences; chiefly among them is the fact that the nuclear polarization in CdTe is insensitive to light helicity and excitation energy (above 1.5 eV). Such results are incompatible with predictions derived from the 'traditional' OP theory where the resulting nuclear polarization—ultimately a byproduct of the optical selection rules of direct semiconductors—is expected to exhibit a strong change upon reversal of light helicity. While further experiments are mandatory, spin dependent recombination via shallow paramagnetic centers near the sample surface seems a plausible nuclear polarization mechanism, particularly if, as suggested by time-resolved optical measurements, the electron spin lifetime is shorter than the recombination time. Interestingly, surface spin-dependent recombination not only is consistent with the observed helicity and photon energy dependencies but could also be a factor behind the fast thermal decay (because the NMR signal is roughly expected to reflect the spin alignment of the paramagnetic centers driving the process).

The reasons why our results differ from those reported previously[67] remain presently unknown to us though we speculate that a different type of impurity is present in our samples. As a matter of fact, we note that CdTe surfaces have proven very sensitive to preparation conditions[80]: For, example, x-ray photoelectron spectroscopy studies of methanol-etched CdTe surfaces reported the preferential formation of TeO_2 at

the surface upon exposure to the ambient; little or no oxidation was observed, however, in specimens etched in citric acid.[81] Given this scenario, several strategies seem at hand to shed light on the spatial location and, ideally, the nature of these impurities. The most straightforward seems to be the search of OPNMR signals in thinner CdTe films, but the increased density of dislocations, vacancies and other lattice defects is likely to make comparison with our present results more difficult. Alternatively, one could 'passivate' the surface of a ~ 1 μ, high-quality CdTe film with the subsequent growth of a 'capping layer' tens of nanometers thick; note that with the selection of a transparent, wider-bandgap material such as ZnSe, differences in the observed behavior are likely to expose the role that surface impurities play in the CdTe OP process.

The authors are indebted to Prof. Jeffrey Reimer for helpful discussions. We acknowledge support from NSF through grants CHE-0545461 and ECS-0608763. C.A.M. thanks the Research Corporation for support through the Cottrell Scholar program.

Chapter 6

Strategy for optical detection of NMR

6.1 Overview

Nuclear Magnetic Resonance could certainly be a premier tool in cell microscopy: unlike any other technique, NMR is unique in allowing the generation of images with various kinds of contrast, and therefore images with different information content In addition, NMR spectroscopy has reached a maturity and flexibility – manifested in the exquisite control of the nuclear spin evolution – that remain unparalleled by other analytical methods. Multidimensional high-resolution spectroscopy is today routinely used (in the liquid *and* solid state) to unveil complex molecular structures and this capability could prove groundbreaking if samples having sub-microscopic (effective) dimensions could be efficiently probed.[82]

Unfortunately, these features cannot be fully exploited at present because NMR lacks the sensitivity essential to high-resolution screening.†,[83] The origin of this limitation is twofold: First, in "conventional" NMR, the signal to noise ratio is proportional to the nuclear magnetic polarization of the sample, which, as is well known, represents only a small fraction of the attainable maximum (~10^{-4} for protons in a 14 T magnet at 300 K). Second, Faraday induction is, in general, a rather poor detection method since, *even with maximum polarization*, the minimum number of spins needed to induce a measurable signal is invariably large.[84]

Although experiments performed at lower temperatures and/or higher fields can partly mitigate these problems, spectroscopists have resorted to other more efficient schemes. In semiconductors, for example, "Optical Pumping" and "Faraday Rotation" have been combined to detect the nuclear magnetization with unparalleled sensitivity.

6.2 Optical Faraday rotation (OFR)

OFR is one among a number of 'magneto-optical' phenomena observed to date. One main difference between OFR and natural circular birefringence is that OFR can be induced by an external magnetic field and/or a net magnetization in *any* material. Meanwhile the OFR rotation depends on the relative direction of light beam and the external magnetic field, and will be changed upon reversal of either one.

---

† The spatial resolution attained in standard MRI machines roughly reaches 0.5 to 0.1 mm in the best systems. Microcoil technology (alongside with a careful design of the rf-pulse sequence) has pushed this limit down to roughly 1 μm.

Concretely speaking, when a linear polarized light passes through a medium, the polarization plane of light will rotate a certain angle. That rotation depends on the intensity of the component of the magnetic field in the light propagation direction, light wavelength as well as medium itself. The relation can be written as,

$$\theta = \nu L(\vec{B} \cdot \hat{k}_0) \tag{6.1}$$

where ν represents the Verdet constant of the medium, L is the length of path on which light and magnetic field interact, $\hat{k}_0$ is the unit wave vector and $\vec{B}$ is the external magnetic field.

It is worth pointing out that the external magnetic field is not indispensable to induce an OFR rotation. In case of paramagnetic material, the optical rotation is also observed in absence of an external field $\vec{B}$, which can be interpreted as resulting from a field-induced alignment of the net magnetic moment of the molecule. This is the principle behind time-resolved OFR, used extensively to investigate semiconductors[28].

6.3 Hyperfine coupling between the electrons and nuclear spins

The interaction between the electrons and the nuclear spin reservoirs is called hyperfine coupling. For an electron of total angular momentum $J = L + S$ interacting with a nuclear spin I_n at a distance r_n, according to Abragam[85], the corresponding Hamiltonian can be written as:

$$H_{hf} = \frac{\mu_0}{4\pi} g^* \mu_B \hbar \sum_n \gamma_n < I_n > \times \{\frac{\vec{L}}{r_n^3} - \frac{\vec{S}}{r_n^3} + 3\frac{\vec{r}_n(\vec{S} \cdot \vec{r}_n)}{r_n^5} + \frac{8}{3}\pi \vec{S}\delta(\vec{r}_n)\} \tag{6.2}$$

The sum takes into account contributions from all nuclei in the molecule and $< I_n >$ represents the ensemble average over the nuclear spin. As usual μ_B and g^* are Bohr magneton and effective electron g-factor in the system respectively. The first three terms give the hyperfine coupling due to the dipolar interactions between nuclear spin and the electronic magnetic moments. The last term, often known as the "Fermi contact" term, relates to the direct interaction of the nuclear spin with the electron spin and is only non-zero for states with a finite electron spin density at the position of the nucleus (those with unpaired electrons in *s*-subshells), and for s-type electrons, Fermi contact term usually plays a dominant role in the whole hyper coupling.

6.4 Time-resolved OFR----pump-probe technique

The main advantage of pump-probe technique lies in that it's capable of detecting the events that happen over the span of nanoseconds. The electron spin relaxation time in semiconductors typically is on the order of hundreds of picoseconds, therefore pump-probe technique is an excellent option to detect these ultrafast events. Concretely speaking, in case of a semiconductor sample, a strong circularly polarized pump pulse first builds up a field-induced alignment of the net magnetic moment of the electrons in the sample, and then a time-delayed linear polarized pulse follows the pump pulse and passes through that "pumped" area. The more electrons are populated to the excited state, the greater net magnetic moment in the "pumped" area is. The number of electrons in the excited state hence will be determined by monitoring the probe light OFR. The delay time interval between the pump pulse and probe pulse can be varied by a "delay line"

device on the probe light path. Initially pump light and probe light are split from the same laser source by a beam splitter, and then probe light is sent off to travel down a different path. The "delay line" which lengthens the path the probe light has to travel relative to the pump light is included on this path. If the delay line increases the probe light path ΔL, it takes $\Delta t = \Delta L / c$ that longer for the probe pulse to reach the sample than the pump pulse. This means you can probe the sample Δt after it has been pumped. If you keep doing that you can probe 0, Δt, $2\Delta t$, $3\Delta t$ … after it has been pumped. In our case, this renders the time evolution of electron spin decay process in the semiconductor. It is worth mentioning that the pump pulse is repeated at constant rate (laser repetition rate) which is low enough to ensure all electrons have returned to their ground state before the next pump pulse arrival.

In order to reduce the noise due to laser intensity fluctuations, pump light and probe light are usually modulated at as high as possible frequencies. The underlying reason behind this is: This type of noise is dominant in the range from several Hz to several hundred Hz; if the signal is modulated at a relative high frequency (several kHz to hundred kHz), we can easily distinguish signal and this type of noise via a lock-in amplifier. In our experimental setup, a photo-elastic modulator (PEM) is used to sinusoidally vary the 'pump' amplitude (at 100 kHz) whereas a mechanical chopper modulates the probe light at 5 kHz. Detection of the signal is carried out via a lock-in detector at the frequency difference. This strategy allows for the removal of undesired 'background' signals that originate in light scattered from the 'pump' pulse and is crucial in situations where the signal-to-noise ratio is weak (as is usual in reflection mode). A

computer is used to vary the position of the delay line synchronously with the lock-in acquisition allowing for an automated acquisition of the sample response.

A high degree linear polarization of the incident laser beam can be easily guaranteed by a simple linear polarizer, but in practice the detection of the actual rotation of the polarization plane upon traversing the sample is *not* that straightforward. One possibility is to use 'crossed' polarizers geometry, which means a second polarizer oriented perpendicularly relative to the first one and the detector is right after the second polarizer. It seems we were able to obtain non-zero signals only after the field-induced OFR rotation of the light polarization occurred. And if the magnetic field is off, we should achieve a perfect extinction condition by reorienting one of the polarizers. Yet, in fact this configuration hardly renders a perfect extinction condition even in the absence of instrumental imperfections for a number of reasons: chief among them is that, in addition to circular birefringence, the sample will also display differential absorption. As a result, light leaving the sample has become elliptically polarized already.

A more sophisticated setup sketched in Fig. 6.1 can successfully avert this problem. The main idea is that we equally split the polarization of probe light into two orthogonal directions, and then inspect the difference between these two components to determine the rotation of polarization plane. Concretely speaking, the second linear polarizer is replaced by a polarizing beam-splitter cube (Glan-laser BS). Within a wide wavelength range, only incoming light polarized along one of the two axes is fully transmitted; light polarized along the orthogonal direction is deflected to the side. With the aid of a half-wave plate preceding the beam splitter, it is customary to set the axis of polarization of incoming light at 45 degrees relative to the beam-splitter orthogonal axes

(bridge 'balancing'). When sample magnetization introduces additional rotation of the beam polarization, identical photodiodes placed at each branch of the polarizer provide a differential signal D whose amplitude is immune, for example, to partial circular polarization. Further, this detection strategy is less sensitive to variations of the laser intensity (usually the dominant source of noise) because both branches of the polarizer are affected in almost identical ways.

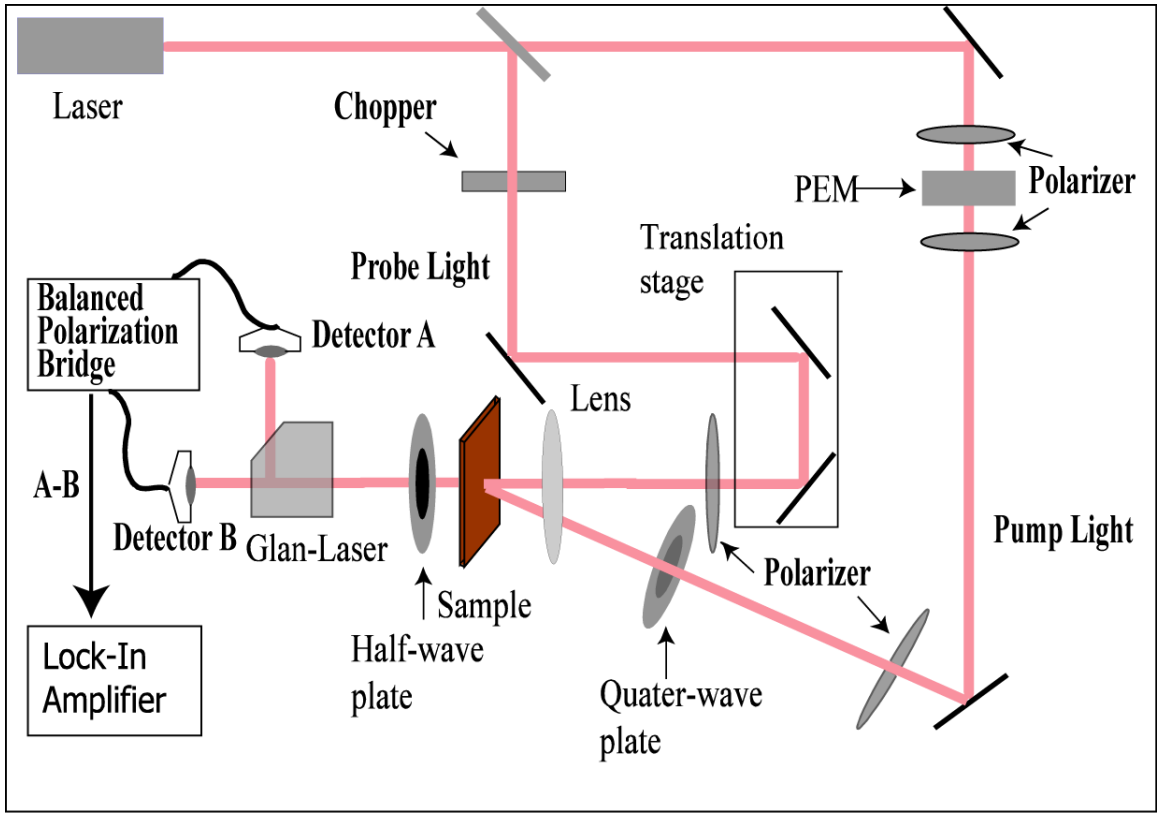

Fig. 6.1: Schematic experimental setup of pump-probe technique with a 'bridge' configuration for detection of Faraday rotation

Time-resolved OFR measurement (transmission mode) of the electron spin lifetime on a 200 μm thick GaAs film at room temperature in absence of an external

magnetic field is shown in Fig 6.2. The wavelength of the pump light is set just above the absorption edge of GaAs.

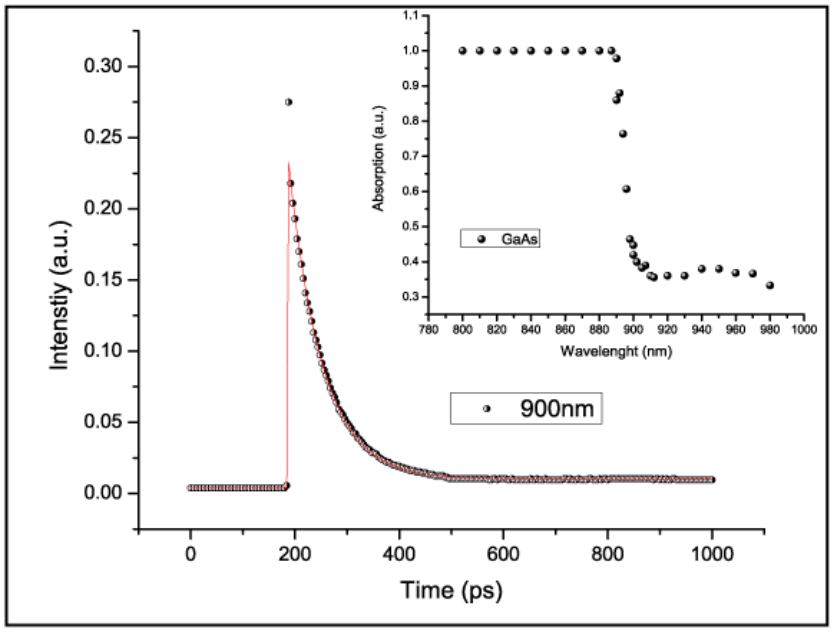

Fig 6.2 Time-resolved Faraday rotation (TRFR) measurement of electron spin lifetime in a semi-insulated GaAs single crystal in absence of external magnetic field at room temperature

In presence of an external magnetic field $\vec{B}_0$ along z-axis, the electronic magnetization $\vec{S}$, induced by the strong circularly polarized 'pump' light propagating along x-axis (Voigt geometry), will start to process about $\vec{B}_0$. Here I'd like to get into a little more details of the electronic magnetization $\vec{S}$. First let us consider the 'pump' light excites one electron from the valence band to the conduction band, the promoted electron is in a coherent superposition of basic states defined by the external field, and the coherence evolution of this superposition results in a phase difference between the two energy eigenstates. The semi-classic treatment views this as the Larmor procession of an electron spin about the external field. A number of possible events cause the amplitude of

this processing spin vector decay, such as spin-spin scattering, local magnetic impurities, spin-orbit scattering due to phonons and impurities or finite lifetime effects caused by optical recombination with a hole. In practice, what we deal with is an ensemble of electron spins. The electronic magnetization $\vec{S}$ is yielded by constructively adding the optically-excited electron spins. If all the conduction electrons are identical, then the decay of $\vec{S}$ will purely stem from intrinsic spin decoherence of individual electrons, however the inhomogeneous effects, such as variation in g-factors or local magnetic fields can further speed up the decay of $\vec{S}$, which is characterized the experimental transverse spin relaxation time T_2^*. Because the Faraday rotation θ_F is proportional to the strength of $\vec{S}$, one hence can interrogate the electron spin Larmor procession by monitoring the linearly polarized probe light. As shown in Fig 6.3, the time-resolved Faraday rotation has the form

$$\theta_F = A\exp(-\frac{t}{T_2^*})\cos(\omega_L t) \tag{6.3}$$

where the electronic Larmor frequency $\omega_L = \frac{g_e^*\mu_B B_{total}}{\hbar}$, A represents an arbitrary constant. B_{total} indicates the total magnetic fields which electron spins experience. As elaborated before, the electron spins and nuclear spins are connected via the hyperfine coupling. In case a change of net magnetization induced by nuclear spins (for instance, optically hyper-polarizing nuclear spins), the electrons in proximity to those nuclear spins will process at different frequency. Finally this electronic Larmor frequency shift can be used as a highly sensitive method to probe the local nuclear magnetization. Salis et al. have

harnessed the high sensitivity of this scheme to reconstruct nuclear magnetic resonance spectra in a 10 nm quantum well.[86]

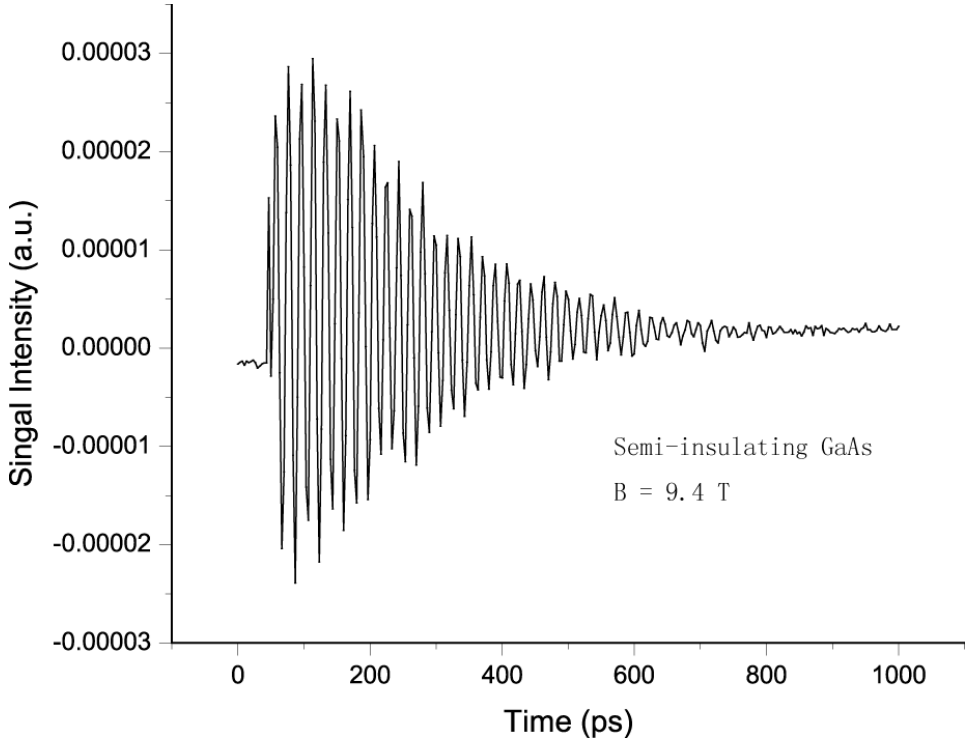

Fig 6.3 TRFR measurement of electronic magnetization oscillation decay in a semi-insulated GaAs single crystal with Voigt geometry, $\vec{B}_0$ =9.4 T, temperature T = 6 K.

From a practical standpoint, there are still some factors concerning samples we should consider to tap the full potential TRFR detection. First, the electron transverse spin life time T_2^* plays a critical role in this scheme, since the longer the spins keep their phase, the more obvious of the frequency shift can be observed. The time during which the electronic magnetization decays to an extent of signal still distinguishable actually imposes the low probing limit of this scheme. Ideally we'd like to extend T_2^* as long as possible. Awschalom et al. have carried out many studies focused on T_2^* measurements in bulk and quantum confined semiconductors. One among them which is particularly

relevant to our experiments is T_2^* measurements in n-GaAs single crystals. The measurements employ Si-doped GaAs single crystals with doping densities ranging from $n = 1\times10^{16}$ cm^{-3}, $n = 1\times10^{18}$ cm^{-3} and $n = 5\times10^{18}$ cm^{-3}, respectively. A measurement in semi-insulating GaAs crystal was carried out as the reference. As shown in Fig 6.4, the spin lifetime is not a monotonic function of doping density, abruptly increasing between the $n = 0$ and $n = 1\times10^{16}$ cm^{-3} samples and steadily decreasing thereafter. Apparently the sample with $n = 1\times10^{16}$ cm^{-3} doping density will be desirable for TRFR detection use.

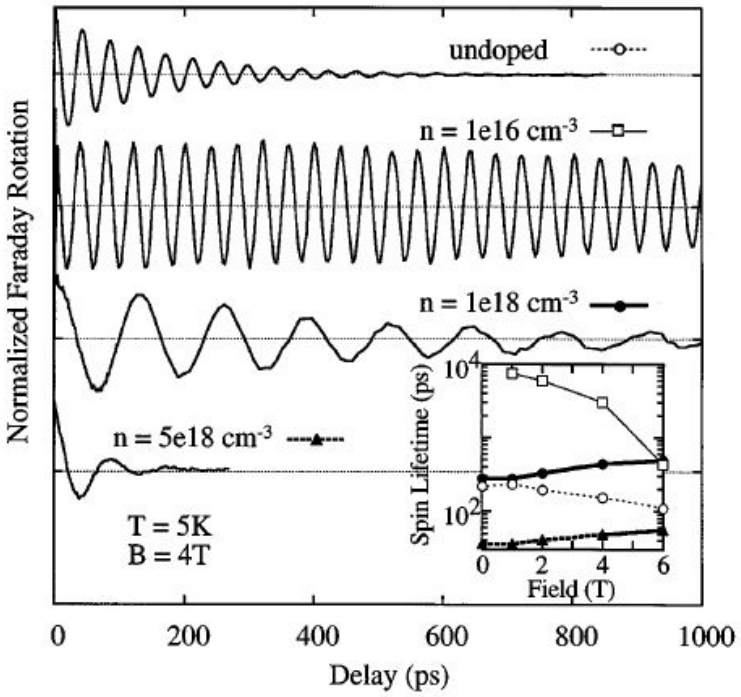

Fig 6.4 TRFR for undoped and n-type GaAs at B = 4 T. Taken from J. M. Kikkawa and D. D. Awschalom, *Phys. Rev. Lett.* 80, 4313 (1998)

Secondly, we will gain higher detection sensitivities in samples with big g-factor. Although GaAs will certainly be the primary choice due to the extensive studies, other semiconductors, such as CdTe[87], InP[88-89,90,91], CdS[92] and CdSe[93], shouldn't be discarded

exploring. For example, the g-factor for the semi-insulating GaAs single crystal is -0.44 at liquid Helium temperature, however semi-insulating CdTe single crystal has a much bigger g-factor (1.68) at the same temperature, which has been shown in Fig 6.5.

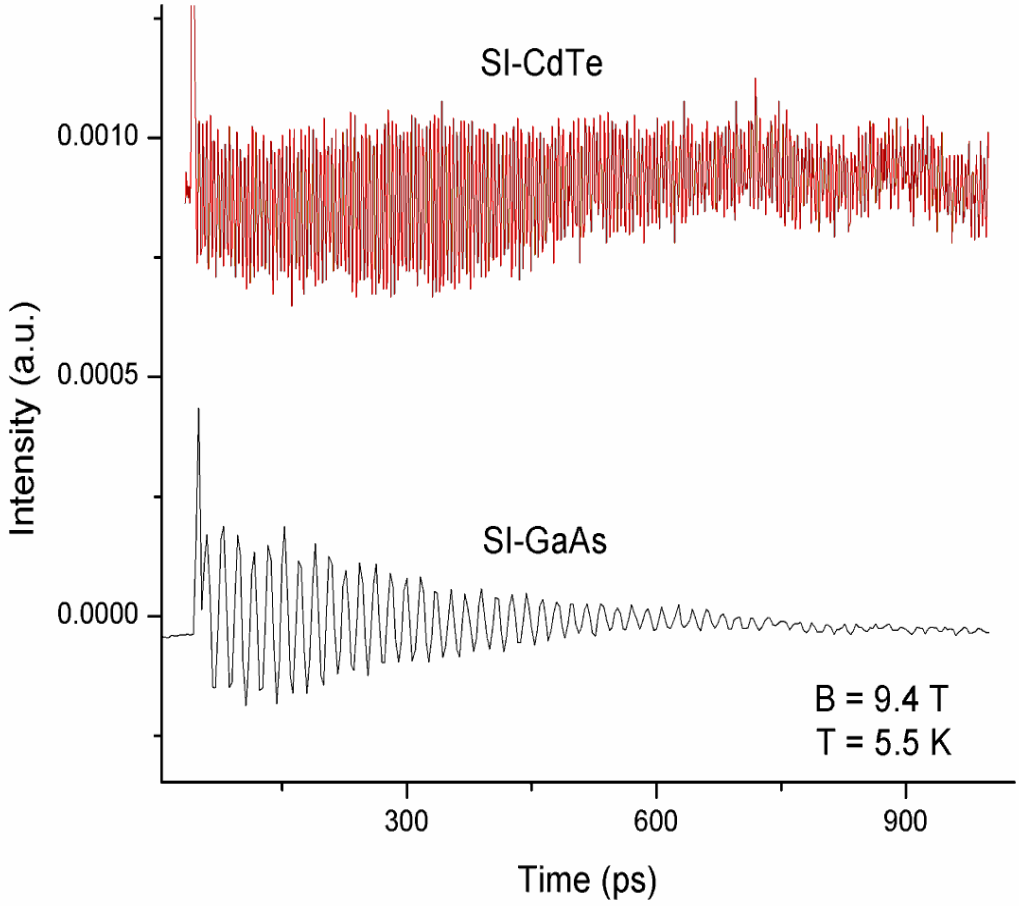

Fig 6.5 TRFR measurements for undoped GaAs and CdTe single crystals at T = 5.5 K and B = 9.4 T.

6.5 Ultimate Goal----Integrating TRFR and OP with NMR

If the extremely sensitive TRFR detection could be combined with the fairly matured modern NMR hardware, the state-of–the-art NMR sequences, and the optical hyperpolarization of nuclear spins technique, then the applications of NMR will be remarkably expanded. Towards this end, we designed and finished a cutting-edge optical NMR probe which is shown in fig 6.6. The assembly of this unit was carried out in collaboration with Attocube AG, a leading company specialized on low temperature optical microscopy. As designed, the pump and probe beams following two adjacent but parallel paths are reflected onto the bore of the magnet and then get into the cryostat through two clear quartz windows at its end. The adjustable broadband mirrors and prism mounted on the titanium stage conduct both beams in and out of the system. Two identical aspheric lenses are co-focally placed on the sample region, capable of focusing the beams on a diffraction-limited spot on the sample. This design has taken the requirement of TRFR in using ultrafast laser pulses into consideration, because no significant distortions are introduced neither in the shape and duration of the light pulse nor in its polarization (as is the case, for example, when long optical fibers are used to channel light onto the sample from external sources). In addition, the configuration of the optical mounts will be fairly flexible, which, in turn, will allow us to alter the geometry of the sample illumination.

The sample is usually glued with low-temperature grease on a sapphire plate which is mounted an aluminum shaft. An rf split coil composed of two flat, separate spirals provide a homogeneous radio-frequency field in the vicinity of the sample without interfering with the light beams trajectories. The rf coil is connected to a set of low-temperature variable capacitors that afford independent matching and tuning of the

resonant circuit at two simultaneous frequencies. The high frequency channel is designed to be resonant on ^{1}H (or ^{19}F) whereas the low frequency channel can be set to operate with a broad range of lower-gyromagnetic-ratio nuclei. Attocube AG also integrated a set of backlash-free nanopositioners into this unit. Those nanopositioners enable us to 3D manipulate sample position as coarse steppers (over a range of up to 0.5 cm) or as fine scanners (3 nm-resolution) at the same time.

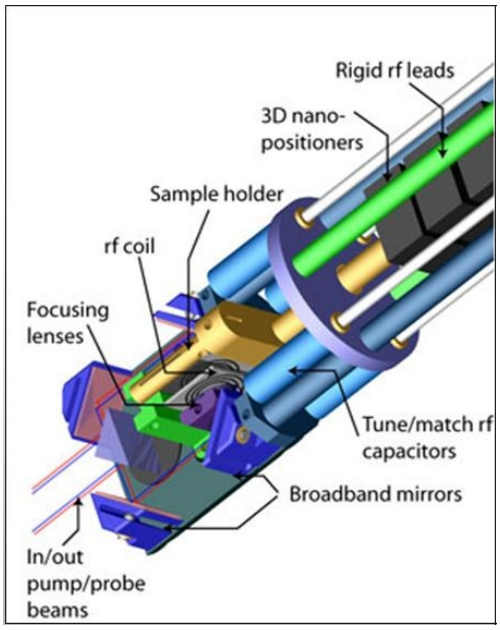

Fig 6.6 A CAD rendition of the optical NMR probe designed by Prof. Matthias Lenzner

NMR technique has been remarkably developed ever since NMR phenomenon was first described and measured by Isidor Rabi in 1938. Along with the tremendous progress in high field magnet, spectrometer hardware as well as the state–of–the–art pulse sequences, NMR unarguably becomes more and more powerful, yet the traditional low sensitive Faraday detection remain no substantial change. As a result, the low

sensitivity has currently become the main obstacle on the NMR developing road. Optical detection's unparalleled high sensitivity makes it become a very promising candidate to succeed the Faraday detection. Optical reading of the electronic Larmor frequency in the semiconductor by using TRFR to probe the sample magnetization seems a very appealing one among the optical detections. In addition, the extensive studies of optical hyperpolarization of nuclear spins in semiconductors are also a big plus as to achieving our ultimate goal. Certainly, the practical integration of optical detection and optical hyperpolarization with modern NMR is still quite challenging, however the steady progress in the area of nanotechnology and optical hyperpolarization makes us quite positive with this goal.

Publication List

- "Helicity-independent optical pumping of nuclear magnetization in bulk CdTe", **W. Dong**, B. Li, CA Meriles, *Phys. Rev. B* **80**, 045211 (2009)
- "Detection of long-range dipole-dipole interactions between nuclear spins in distant solids", **W. Dong**, CA Meriles, *Chem. Phys. Lett.,* 470, 313 (2009).
- "Indirect detection of NMR via geometry-dependent dipolar fields, revisited", **W. Dong**, CA Meriles, *J. Magn. Reson*. 186, 330 (2007)
- "Indirect detection of Nuclear Magnetic Resonance via geometrically-induced long-range dipolar fields", CA Meriles, **W. Dong**, *J. Magn. Reson*. 181, 331 (2006)

Bibliography

[1] C.A. Meriles, "Optically-detected Nuclear Magnetic Resonance at the sub-micron scale", *J. Magn. Reson*. **176,** 207 (2005).

[2] M.H. Levitt, "Demagnetization field effects in two-dimensional solution NMR", *Concepts Magn. Reson*. **8**, 77-103 (1996).

[3] A. Vlassenbroek, J. Jeener, P. Broekaert, "Macroscopic and microscopic fields in high-resolution liquid NMR", *J. Magn. Reson. Ser. A* **118**, 234-246 (1996).

[4] D.G. Cory, J.B. Miller, R. Turner, A.N. Garroway, "Multiple pulse methods of 1H NMR imaging of solids: second averaging", *Mol. Phys.* **70**, 331(1990).

[5] W. Zhang, D.G. Cory, "First direct measurement of the spin diffusion rate in a homogeneous solid", *Phys. Rev. Lett.* **80**, 1324 (1998).

[6] U. Haeberlen, in *High-Resolution NMR in solids. Selective Averaging* (Academic Press, New York, 1976).

[7] M. Bruchez, J. Moronne, P. Gin, S. Weiss, A.P. Alivisatos, "Semiconductor nanocrystals as fluorescent biological labels", *Science* **281**, 2013 (1998).

[8] W.C.W. Chan, S. Nie, "Quantum Dots bioconjugates for ultrasensitive nonisotipic detection", *Science* **281**, 2016 (1998).

[9] A.J. Moulé, M.M. Spence, S.I. Han, J.A. Seeley, K.L. Pierce, S. Saxena, A. Pines., "Aplification of xenon NMR and MRI by remote detection", *Proc. Natl. Acad. Sci. USA* **100**, 9122-9127 (2003).

[10] G.M. Leskowitz, L.A. Madsen, D.P. Weitekamp, "Force-detected magnetic resonance without field gradients", *Sol. Stat. Nucl. Magn. Reson*. **11**, 73-83 (1998).

[11] M. Rosay, J.C. Lansing, K.C. Haddad, W.W. Bachovchin, J. Herzfeld, R.J. Temkin, R.G. Griffin, "High-frequency dynamic nuclear polarization in MAS spectra of membrane and soluble proteins", *J. Am. Chem. Soc*. **125**, 13626-13627 (2003).

[12] G. Deville, M. Bernier, J.M. Delrieux, NMR multiple echoes observed in solid ^{3}He, Phys. Rev. B 19 (1979) 5666 – 5688.

[13] H.T. Edzes, The nuclear magnetization as the origin of transient changes in the magnetic field in pulsed NMR experiments, *J. Magn.Reson.* 86 (1990) 293.

[14] R. Bowtell, Indirect detection via the dipolar demagnetizing field, *J. Magn. Reson*. 100 (1992) 1.

[15] W. Richter, S. Lee, W.S. Warren, Q. He, Imaging with intermolecular zero-quantum coherences in solution nuclear magnetic resonance, *Science* 267 (1995) 654.

[16] X.P. Tang, C.L. Chin, L.S. Bouchard, F.W. Wehrli, W.S. Warren, Observing Bragg-like diffraction via multiple couple nuclear spins, *Phys. Lett. A* 326 (2004) 114.

[17] R. Bowtell, S. Gutteridge, C. Ramanathan, Imaging the long-range dipolar field in structural liquid state samples*, J. Magn. Reson.* 150 (2001) 147.

[18] W.S. Warren, W. Richter, A.H. Andreotti, B.T. Farmer, Generation of impossible cross peaks between bulk water and biomolecules in solution NMR, *Science* 262 (1993) 2005.

[19] J. Granwehr, J.T. Urban, A.H. Trabesinger, A. Pines, NMR detection using laser-polarized xenon as a dipolar sensor, *J. Magn. Reson.* 176 (2005) 125.

[20] S.M. Brown, P.N. Sen, D.G. Cory, Scaling Laws in NMR scattering via dipolar fields, *J. Magn. Reson.* 154 (2002) 154.

[21] Oil and water longitudinal relaxation times where determined through standard inversion-recovery pulse sequences; this experiment yielded 1.6 s and 2.4 s respectively.

[22] A set of Bloch equations modified to include non-linear effects due to the nuclear dipolar field has been numerically solved applying a fourth order Runge-Kutta algorithm. Spins were distributed on a cartesian grid that reproduced the geometry discussed in this paper.

[23] M. Dovers et al., *Phys. Rev. Lett*. **61**, 1650 (1988).

[24] J.A. Nesteroff, Y.V. Pershin, V. Privman, *Phys. Rev. Lett*. **93**, 126601 (2004).

[25] S.A. Crooker et al., *Phys. Rev. B* **56**, 7574 (1997).

[26] J.A. Marohn et al., *Phys. Rev. Lett*. **75**, 1364 (1995).

[27] M. Eickhoff, D. Suter, *J. Magn. Reson.* **166**, 69 (2004).

[28] J.M. Kikkawa, D.D. Awschalom, *Science* 473 (2000).

[29] D. Gammon et al., *Science* **277**, 85 (1997).

[30] A set of Bloch equations modified to include non-linear effects due to the nuclear dipolar field has been numerically solved applying a fourth order Runge-Kutta algorithm. Spins were distributed on a Cartesian grid that reproduced the geometry discussed in this paper.

[31] G. Deville, M. Bernier, J.M. Delrieux, NMR multiple echoes observed in solid ^{3}He, *Phys. Rev. B* 19 (1979) 5666.

[32] A. Vlassenbroek, J. Jeener, P. Broekaert, Macroscopic and microscopic fields in high-resolution liquid NMR, *J. Magn. Reson. Ser. A* 118 (1996) 234.

[33] M.H. Levitt, Demagnetization field effects in two-dimensional solution NMR, *Concepts Magn. Reson*. 8 (1996) 77.

[34] S. Vathyam, S. Lee, W.S. Warren, Homogeneous NMR spectra in inhomogeneous fields, *Science* 272 (1996) 92.

[35] R. Bowtell, R.M. Bowley, P. Glover, Multiple spin echoes in liquids in a high magnetic field, *J. Magn. Reson.* 88 (1990) 643.

[36] R. Bowtell, Indirect detection via the dipolar demagnetizing field, *J.Magn. Reson.* 100 (1992) 1.

[37] R. Bowtell, S. Gutteridge, C. Ramanathan, Imaging the long-range dipolar field in structural liquid state samples*, J. Magn. Reson.* 150 (2001) 147.

[38] S.M. Brown, P.N. Sen, D.G. Cory, Scaling Laws in NMR scattering via dipolar fields, *J. Magn. Reson.* 154 (2002) 154.

[39] S.M. Brown, P.N. Sen, D.G. Cory, Nuclear magnetic resonance scattering across interfaces via the dipolar demagnetizing field*, J.Chem. Phys.* 116 (2002) 295.

[40] C.A. Meriles, W. Dong, Indirect detection of Nuclear Magnetic Resonance via geometrically-induced long-range dipolar fields, *J.Magn. Reson.* 181 (2006) 331.

[41] Because the sample magnetic field is to be calculated only on the region occupied by the sensor, it is enough to divide the sample volume into sufficiently small compartments $\mathrm{d}V$ with magnetic moment $\mathrm{d}\mu = \mathrm{M}\mathrm{d}V$, with M the magnetization of the sample (assumed homogeneous). The magnetic field at a given point on the sensor is obtained by co-adding the contributions to the field at a given point from all elementary dipoles $\mathrm{d}\mu$. See, for example, J.D. Jackson, Classical Electrodynamics, third ed., Wiley, New York, 1999, Chapter 5.

[42] The reader is reminded that T_{snr} is the *transverse* relaxation time of the sensor whereas T_{spl} indicates the longitudinal relaxation time of the sample. Therefore, $T_{snr} << T_{spl}$ will be the most common scenario.

[43] W. Dong, C.A. Meriles, *J. Magn. Reson.* 186 (2007) 330.

[44] J.M. Taylor et al., *Nature Phys.* 4 (2008) 810.

[45] P. Cappellaro, J. Emerson, N. Boulant, C. Ramanathan, S. Lloyd, D.G. Cory, *Phys. Rev. Lett.* 94 (2005) 020502.

[46] P. Mansfield, M.J. Orchard, D.C. Stalker, K.H.B. Richards, *Phys. Rev. B* 7 (1973) 90.

[47] W.-K. Rhim, D.D. Elleman, R.W. Vaughan, *J. Chem. Phys.* 59 (1973) 3740.

[48] M. Mehring, Principles of High-resolution NMR in Solids, Springer-Verlag, Berlin, 1983

[49] D. Budker, M. Romalis, *Nature Phys.* 3 (2007) 227.

[50] T.D. Ladd, D. Maryenko, Y. Yamamoto, E. Abe, K.M. Itoh, *Phys. Rev. B* 71 (2005) 014401.

[51] D.P. Burum, W.K. Rhim, *J. Chem. Phys.* 71 (1979) 944.

[52] G.S. Boutis, P. Capellaro, H. Cho, C. Ramanathan, D.G. Cory, *J. Magn. Reson.* 161 (2003) 132.

[53] G. Yusa, K. Muraki, K. Takashina, K. Hashimoto, Y. Hirayama, *Nature* 434 (2005) 1001.

[54] D. Gammon, S.W. Brown, E.S. Snow, T.A. Kennedy, D.S. Katzer, D. Park, *Science* 277 (1997) 85.

[55] S. Matsui, J. *Magn. Reson.* 98 (1992) 618.

[56] H.J. Mamin, M. Poggio, C.L. Degen, D. Rugar, *Nature Nanotechnol.* 2 (2007) 301.

[57] A.K. Paravastu, J.A. Reimer, "Nuclear spin temperature and magnetization transport in laser-enhanced NMR of bulk GaAs", *Phys. Rev. B* **71**, 045215 (2005).

[58] A. Patel, O. Pasquet, J. Bharatam, E. Hughes, C.R. Bowers, "Optical dynamic nuclear polarization in InP single crystal: Wavelength and field dependence of NMR enhancement", *Phys. Rev. B* **60**, R5105 (1999).

[59] A. Brunetti, M. Vladimirova, D. Scalbert, H. Folliot, A. Lecorre, "Effect of holes on the dynamic polarization of nuclei in semiconductors", *Phys. Rev. B* **73**, R121202 (2006).

[60] S. Mui, K. Ramaswany, S.E. Hayes, "Effects of optical absorption on ^{71}Ga optically polarized NMR in semi-insulating GaAs: measurements and simulations", *Phys. Rev. B* **75**, 195207 (2007).

[61] K. Ramaswany, S. Mui, S.E. Hayes, "Light-induced ^{71}Ga shifts in semi-insulating GaAs observed by optically polarized NMR", *Phys. Rev. B* **74**, 153201 (2006).

[62] F. Meier, B.P. Zakharchenya (Eds.), Optical Orientation (Modern Problems in Condensed Matter Science), vol. 8, North-Holland Physics Publishing, Amsterdam, 1984.

[63] C. Weisbuch, C. Hermann, "Optical detection of conduction-electron spin resonance in GaAs, $Ga_{1-x}In_xAs$, and $Ga_{1-x}Al_xAs$", *Phys. Rev. B* **15**, 816 (1977).

[64] A. Abragam, *Principles of Nuclear Magnetism,* Oxford University Press, New York, 1996.

[65] A. Paravastu, S.E. Hayes, B.E. Schwickert, L.N. Ding, M. Balooch, J.A. Reimer, "Optical polarization of nuclear spins in GaAs", *Phys. Rev. B* **69**, 075203 (2004).

[66] Q. Zhan, W. Charles, B. Li, A. Shen, C.A. Meriles, M.C. Tamargo, "Control of crystal orientation of CdTe epitaxial layers grown on (001) GaAs with ZnSe buffer layer by molecular beam epitaxy", *J. Cryst. Growth,* in press.

[67] I.J.H. Leung, C.A. Michal, "Optical enhancement of NMR signals in CdTe", *Phys. Rev. B* **70**, 035213 (2004).

[68] P.J. Coles, "Helicity asymmetry of optically pumped NMR spectra in GaAs", *Phys. Rev. B* **78**, 033201 (2008).

[69] D. Paget, G. Lampel, B. Sapoval, V.I. Safarov, "Low-field electron-nuclear spin coupling in gallium arsenide under optical pumping conditions", *Phys. Rev. B* **15**, 5780 (1977).

[70] P.L. Kuhns, A. Kleinhammes, T. Schmiedel, W.G. Moulton, P. Chabrier, S. Sloan, E. Hughes, C.R. Bowers, "Magnetic-field dependence of the optical Overhauser effect in GaAs", *Phys. Rev. B* **55**, 7824 (1997).

[71] D. R. Lide, Ed,, *Handbook of Chemistry and Physics*, 77th ed. (CRC, Boca Raton, FL, 1996), Ch. 12, pp. 12-98.

[72] J. Tribollet, E. Aubry, G. Karczewski, B. Semage, F. Bernardot, C. Testelin, M. Chamarro, "Enhancement of the electron spin memory by localization on donors in a CdTe quantum well", *Phys. Rev. B* **75**, 205304 (2007).

[73] P.Y. Yu, M. Cardona, *Fundamentals of semiconductors,* Springer-Verlag, Berlin, 1996.

[74] A.A. Sirenko, T. Ruf, M. Cardona, M. Yakovlev, W. Ossau, A. Waag, G. Landwehr, "Electron and hole *g* factors measured by spin flip Raman scattering in CdTe/$Cd_xMg_{1-x}Te$ single quantum wells", *Phys. Rev. B* **56**, 2114 (1997).

[75] D.J. Lepine, "Spin-dependent recombination on silicon surface", *Phys. Rev. B* **6**, 436 (1972).

[76] C. Boehme, K. Lips, "Electrical detection of spin coherence in silicon", *Phys. Rev. Lett.* **91**, 246603 (2003).

[77] R.I. Dzhioev, K.V. Kavokin, V.L. Korenev, M.V. Lazarev, B. Ya. Meltser, M.N. Stepanova, B.P. Zakharchenya, D. Gammon, D.S. Katzer, "Low-temperature spin relaxation in *n*-type GaAs", *Phys. Rev. B* **66**, 245204 (2002).

[78] P. Nahálková, P. Němec, D. Sprinzl, E. Belas, P. Horodysk´y, J. Franc, P. Hlídek, P. Mal, "Spin dynamics in bulk CdTe at room temperature", *Mat Sci Eng B* **126**, 143, (2006).

[79] P.J. Coles, J.A. Reimer, "Penetration depth model for optical alignment of nuclear spins in GaAs", *Phys. Rev. B* **76**, 174440 (2007).

[80] F. Wang, A. Schwarzman, A.L. Fahrenbruch, R. Sinclair, R.H. Bube, C.M. Stahle, "Kinetics and oxide composition for thermal oxidation of cadmium telluride", *J. Appl. Phys* **62**, 1469 (1987).

[81] S.P. Kowalczyk, J.T. Cheung, "XPS investigation of the oxidation of $Hg_{1-x}Cd_xTe$ surfaces", *J. Vac. Sci. Technol.* **18**, 944 (1981).

[82] L. Ciobanu, A.G. Webb, C.H. Pennington, "Magnetic Resonance Imaging of biological cells", *Prog. NMR Spec.* **42**, 69 (2003).

[83] S-C. Lee, K. Kim, S. Lee, J.H. Yi, SW Kim, K-S. Ha, C. Cheong, "One micrometer resolution NMR microscopy", *J. Magn. Reson.* **150**, 207 (2001).

[84] The minimum amount of sample detectable, for example, in Near Field Optical Microscopy serves as a useful reference for comparison. See, for instance, B. Gross Levi, "Progress made in near-field imaging with light from a sharp tip", *Phys. Today* **52**, 18 (1999).

[85] Abragam A. 1970. The Principles of Nuclear Magnetism. Oxford: Oxford University Press.

[86] G. Salis, D.D. Awschalom, Y. Ohno, H. Ohno, "Origin of enhanced dynamic nuclear polarization and all-optical nuclear magnetic resonance in GaAs quantum wells", *Phys. Rev. B*, **64**, 195304 (2001).

[87] I.J.H. Leung, C.A. Michal, "Optical enhancement of NMR signals in CdTe", *Phys. Rev. B* **70**, 035213 (2004).

[88] R. Tycko, "Optical pumping in indium phosphide: ^{31}P NMR measurements and potential for signal enhancement in biological solid state NMR", *Sol. State NMR*, **11**, 1 (1998).

[89] A. Patel, O. Pasquet, J. Bharatam, E. Hughes, C.R. Bowers, "Optical dynamic nuclear polarization in InP single crystal: Wavelength and field dependence of NMR enhancement, *Phys. Rev. B* **60**, R5105 (1999).

[90] C.A. Michal, R. Tycko, "Nuclear spin polarization transfer with a single radio-frequency field in optically pumped Indium Phosphide", *Phys. Rev. Lett.* **81**, 3988 (1998).

[91] A. Goto, K. Hashi, T. Shimizu, R. Miyabe, X. Wen, S. Ohki, S. Machida, T. Iijima, G. Kido, "Optical pumping NMR in the compensated semiconductor InP:Fe", *Phys. Rev. B* **69**, 075215 (2004).

[92] T. Pietrass, M. Tomaselli, "Optically pumped NMR in CdS single crystals", Phys. Rev. B 59, 1986 (1999).

[93] N.T. Bagraev, L.S. Vlasenko, R.A. Zhitnikov, *Sov. Phys. Solid State* **19**, 1956 (1977).